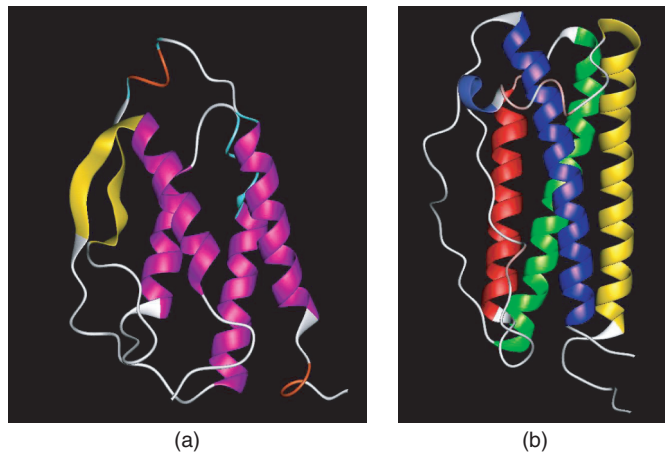


Figure 1.1. Molecular representations comparing the structural complexity of types of parenteral drugs: aspirin (180 Da), penicillin (334 Da), insulin (5808 Da), erythropoietin (36,000 Da), and a monoclonal antibody (MAB) (150,000 Da).



**Figure 1.2.** Ribbon structures of (a) GCSF and (b) GMCSF, illustrating the two major subclasses of four-helix bundle cytokines. Note the shorter helices and longer crossing angles of GCSF.

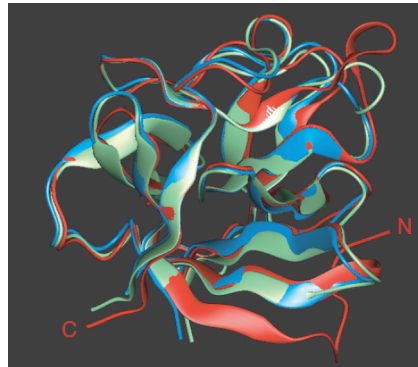
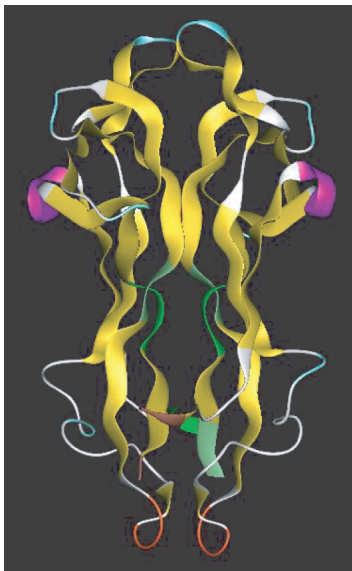


Figure 1.3. Superimposition of the ribbon structures of FGF-1 (green), FGF-2 (blue), and FGF-7/KGF (red). The  $\beta$  trefold is a common structural motif for the FGF family of proteins.



**Figure 1.4.** Ribbon structure of BDNF, representing the structure of the family of proteins termed *cystine knot cytokines*.

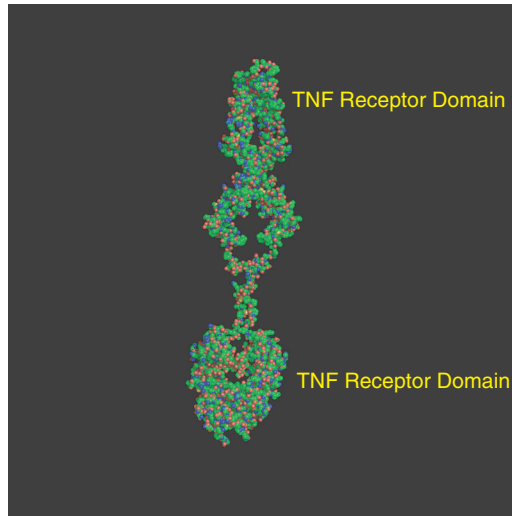
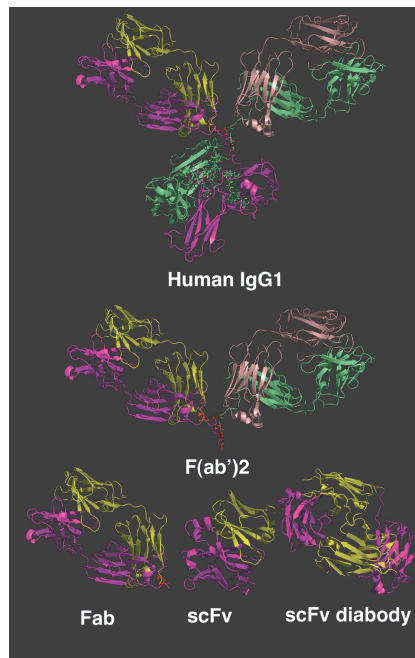
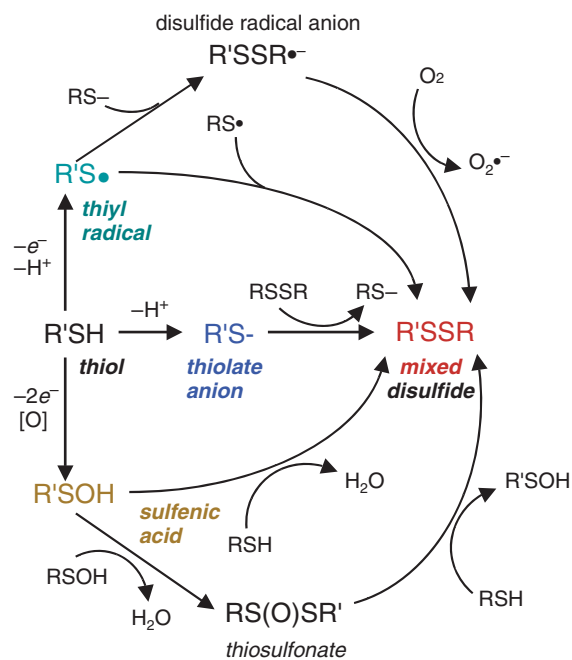


Figure 1.5. Structure of entanercept, a fusion protein with two tumor necrosis factor receptors fused to the Fc of an IgG1.



**Figure 1.6.** Examples of therapeutic antibody constructs. Cartoon structural representations of an intact human IgG1 monoclonal antibody [72] and F(ab')<sub>2</sub> and Fab fragments derived from it, an scFv [72], and an scFv dimer diabody [74]. The heavy chains are shown in magenta and green and light chains, in yellow and wheat. The carbohydrate component of the whole IgG1 molecule is shown as a stick representation and the cysteine residues linking the heavy and light chains are shown in red. The images were produced from PDB files using Pymol (DeLano Scientific, LLC).



**Figure 2.5.** Some pathways for thiol–disulfide exchange. In solution, the thiolate anion ( $RS^-$ ) is the reactive species, though alternative pathways involving the thiyl radical ( $R'S\bullet$ ) or sulfenic acid ( $RSOH$ ) are also possible. Intermolecular thiol–disulfide exchange has been implicated in the formation of covalent protein aggregates. (Adapted from Carballal et al. [188].)

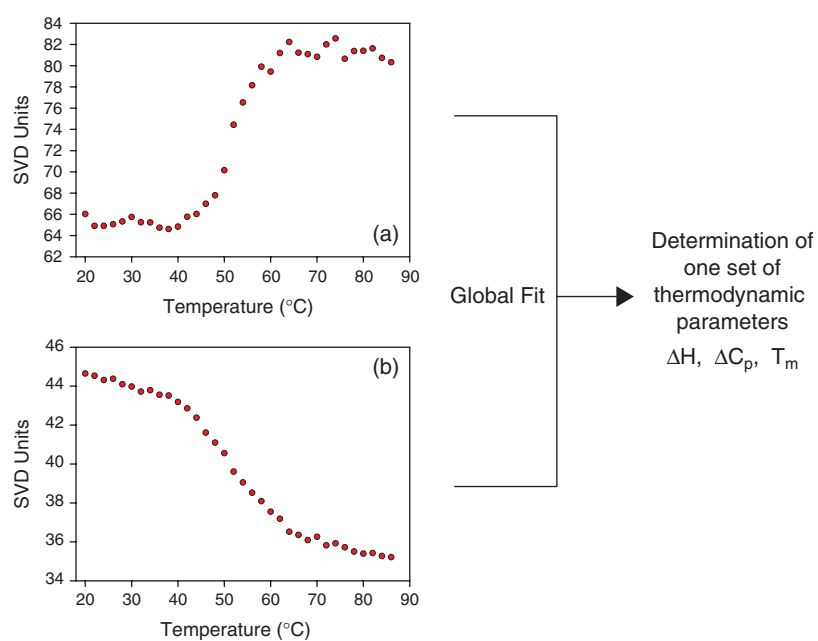


**Figure 5.5.** Schematic showing how a global fit can be done of SVD vectors from different techniques into one set of thermodynamic parameters. Panels (a) and (b) are the SVD unfolding vectors from far-UV CD and fluorescence data, respectively, for a model protein.



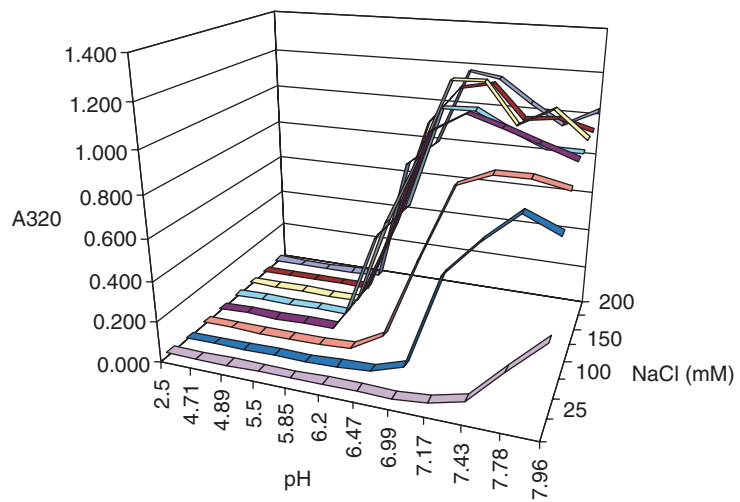


**Figure 6.2.** Effect of pH and NaCl on rhBMP-2 opalescence. Several rhBMP-2 solutions, at 0.2 mg/mL, were titrated to adjust pH and NaCl levels. The resultant solutions were examined by absorbance at 320 nm to assess opalescence.

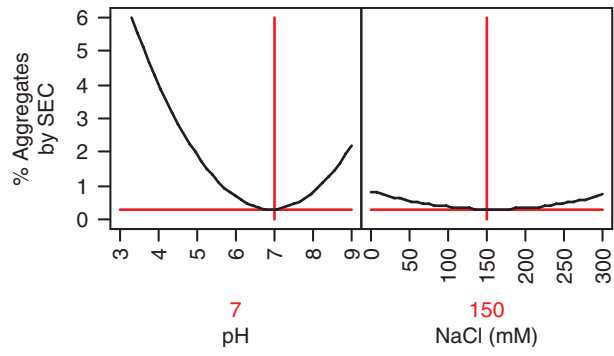


Figure 7.2. Prediction profile on the effect of pH and NaCl concentration on aggregation of an HGS mAb.

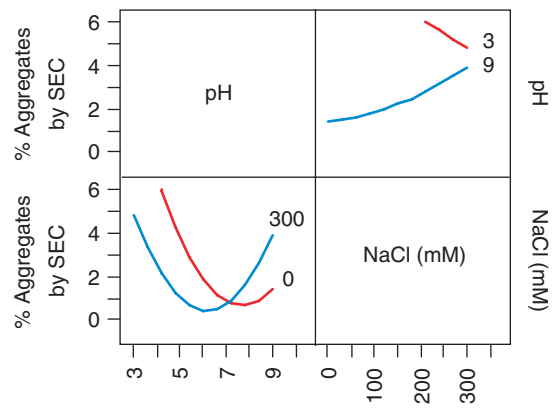
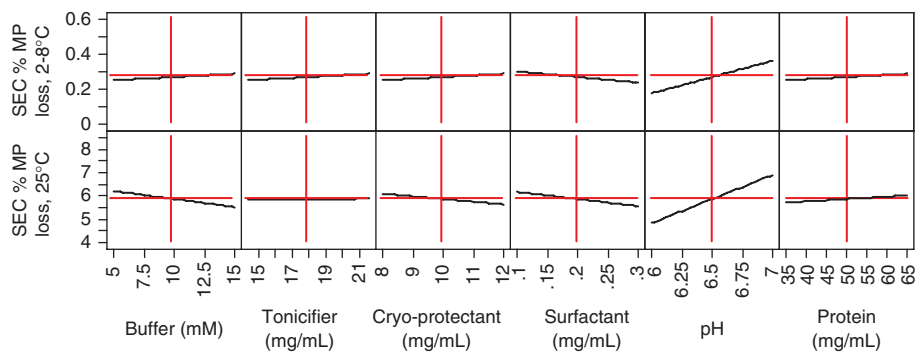


Figure 7.3. Interaction profiles on the effect of pH and NaCl concentration on aggregation of an HGS mAb.



**Figure 7.4.** Effect of formulation components on mAb SE-HPLC.

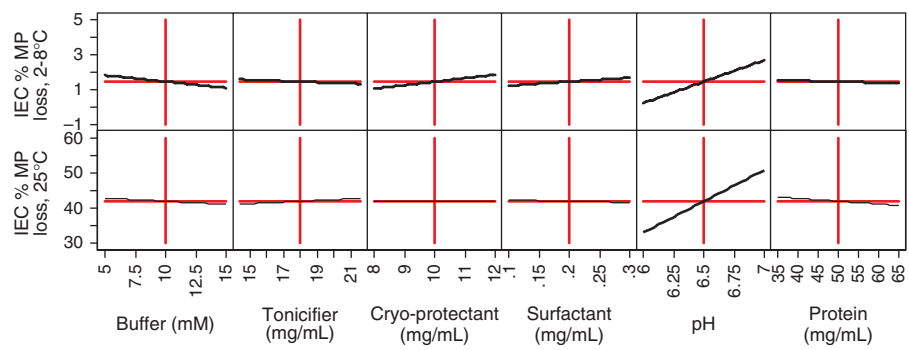
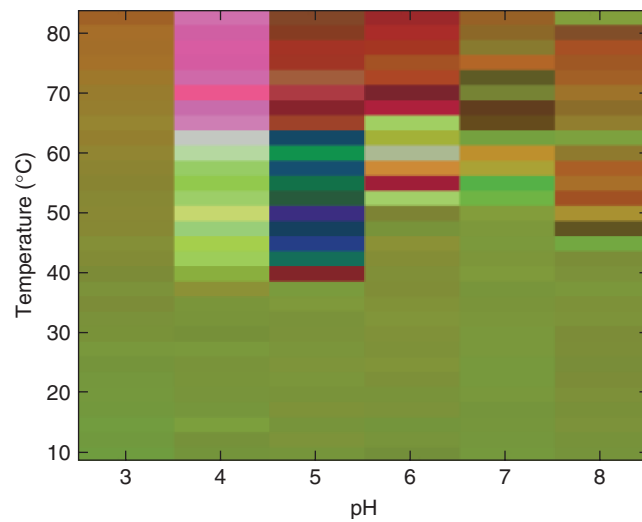
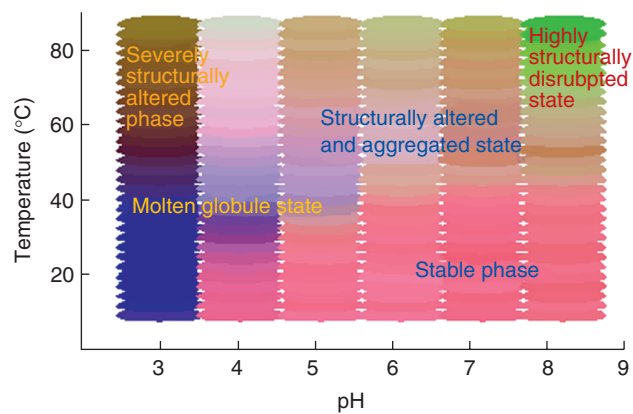


Figure 7.5. Effect of formulation components on mAb IE-HPLC.



**Figure 8.4.** Empirical phase diagram of rPA on a temperature–pH axis constructed using high-resolution second-derivative UV spectroscopy data. The data employed to generate these images was obtained over the pH range of 3–8 (20 mM citrate phosphate buffer,  $I = 0.1$  adjusted with NaCl) and temperatures of 12°C–82.5°C in 2.5°C increments. Blocks of continuous color represent homogenous phases, conditions under which the raw data-derived vectors behave similarly.



**Figure 8.6.** Empirical phase diagram of rPA on a temperature–pH plane on the basis of intrinsic and ANS fluorescence, light scattering ( $OD_{360\text{ nm}}$ ), and CD data. The data employed to generate these images was obtained over the pH range of 3–8 and at temperatures ranging from 12°C to 85°C in 2.5°C increments. Blocks of continuous color represent uniform phases, conditions under which the raw-data-derived vectors behave similarly [24].

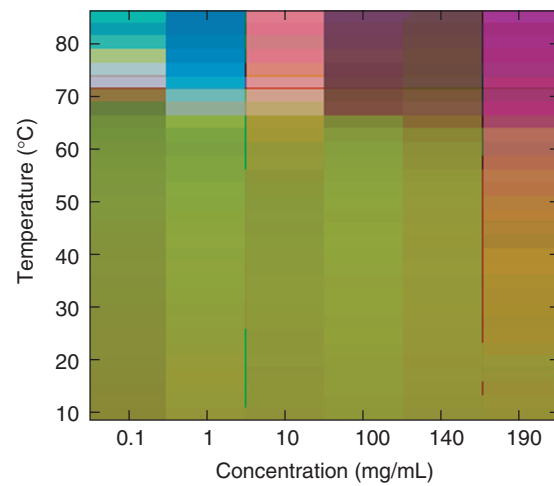


**Figure 8.7.** Empirical phase diagram of a monoclonal antibody on a temperature–protein concentration plane. Each temperature–concentration point on the diagram is constructed from data obtained from fluorescence emission peak position,  $OD_{350\text{ nm}}$ , and second-derivative UV absorbance peak positions of Phe, Tyr, and Trp, and CD molar ellipticity. Note that the concentration axis is not linear [30].



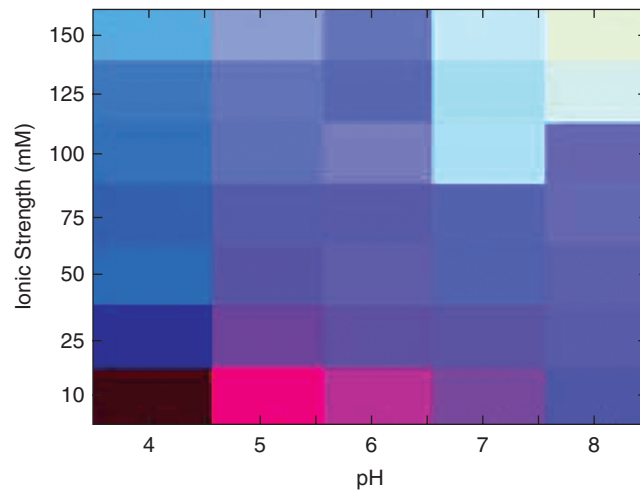


**Figure 8.8.** Ionic strength–pH EPD of a nonviral gene delivery complex. The EPD is generated from dynamic light scattering, CD, and fluorescence studies. Regions of similar color represent similar structural behavior, while the variation in color defines the conditions under which the structure of the gene delivery complex alters [33].

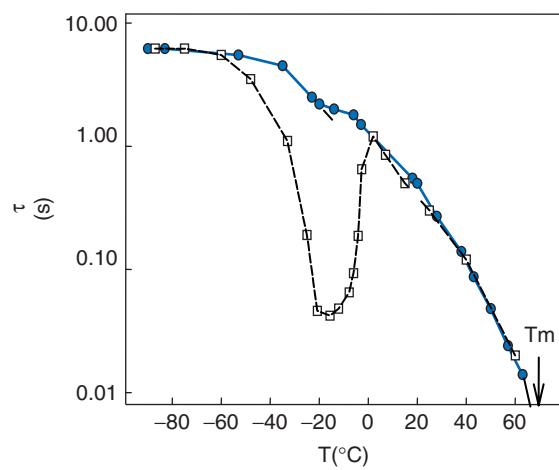


Figure 9.2. Dependence of the average phosphorescence lifetime  $\tau$  of Trp48 of azurin on temperature and solvent composition: (●) 50/50 (w/w) ethylene glycol/potassium phosphate buffer (1 mM, pH 7) and (□) potassium phosphate buffer alone;  $T_m$  is the temperature of thermal denaturation. (Reprinted from Strambini and Gabellieri [26]).

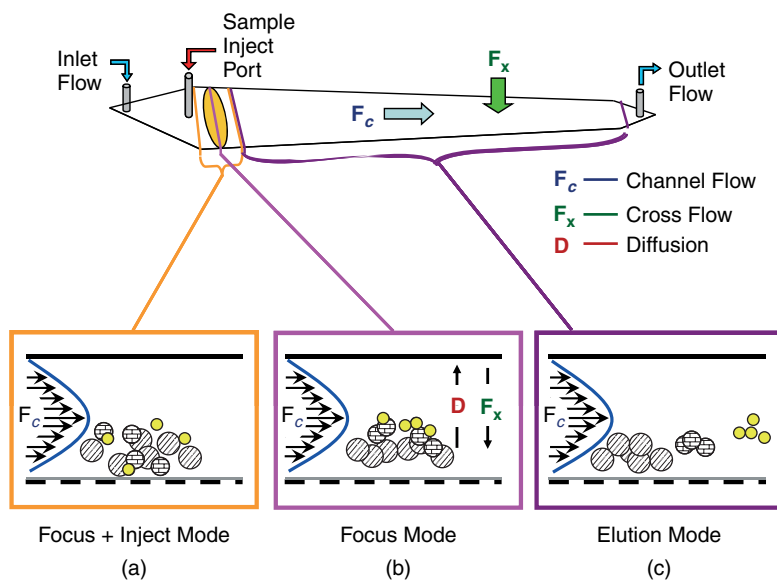
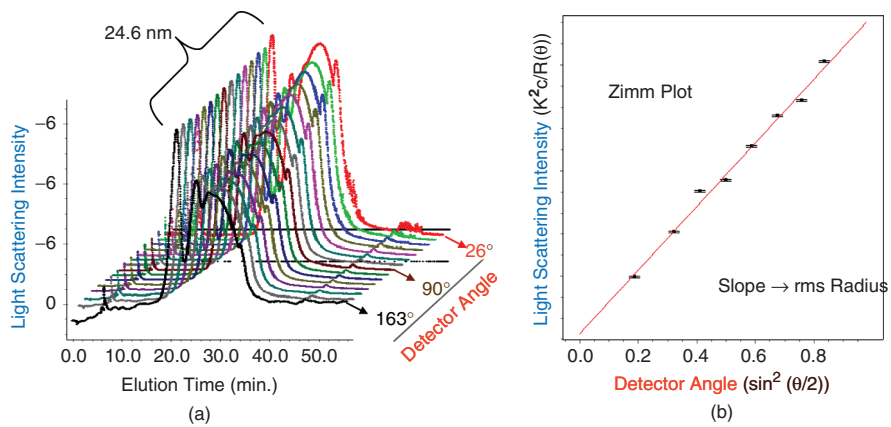


Figure 11.1. A schematic diagram showing the separation mechanism of FFF during the stages of sample injection (a), sample focusing (b), and elution (c).



**Figure 11.2.** (a) An overlay of light-scattering elution profiles from 15 different detection angles ranging from  $26^\circ$  to  $163^\circ$  obtained simultaneously for an FFF-MALS/UV analysis of a VLP preparation; (b) a Zimm plot showing the light-scattering intensity dependence on detection angle for a sampling from a specific elution time. Such a plot is generated for each elution time interval throughout the elution. A RMS radius and molecular weight are calculated from the linear regression of each plot.

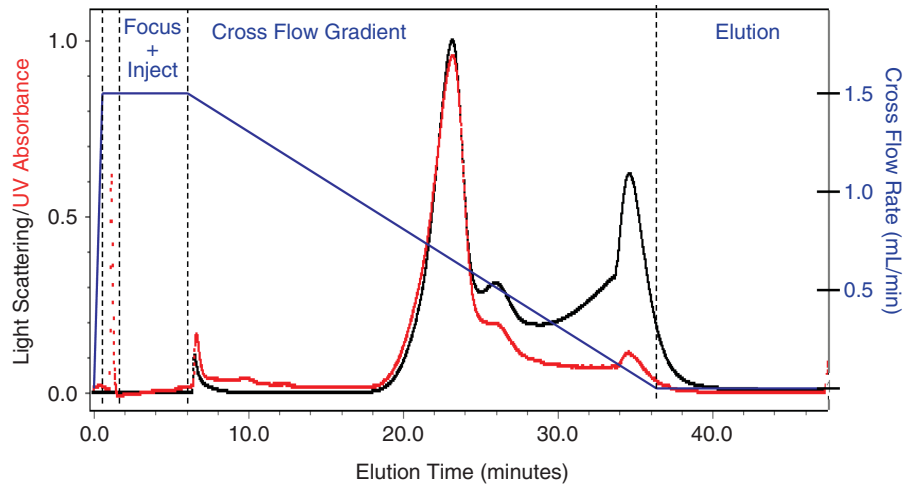
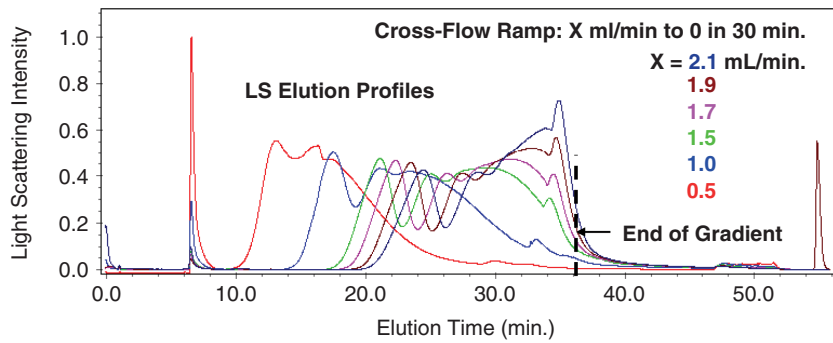
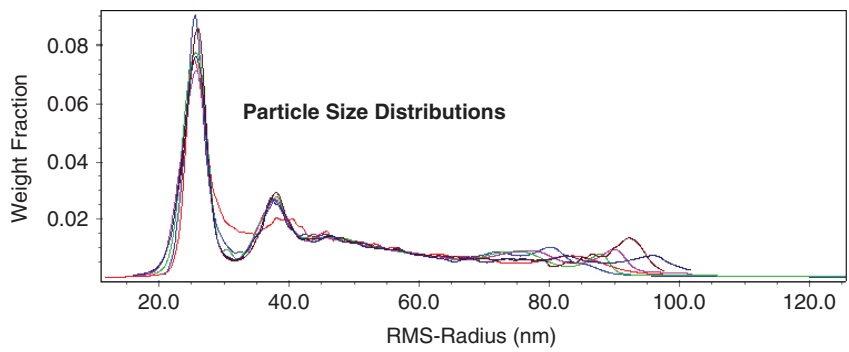


Figure 11.3. An overlay of the 90° light scattering elution profile (black trace) and the 280 nm absorbance elution profile (red trace) for a VLP development preparation. The blue schematic shows the strength of the crossflow throughout the analysis.



(a)



(b)

Figure 11.4. Effects of crossflow strength on sample resolution and aggregation during the FFF elution: (a) comparison of  $90^\circ$  light-scattering elution profiles generated for the same VLP preparation but using different starting crossflow strengths for each analysis; (b) calculated particle size distribution profiles generated from each elution profile of varying crossflow strength displayed in part (a).

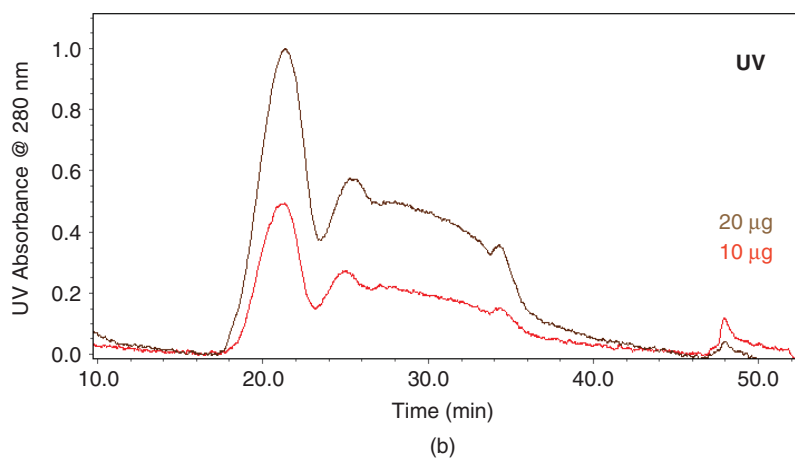
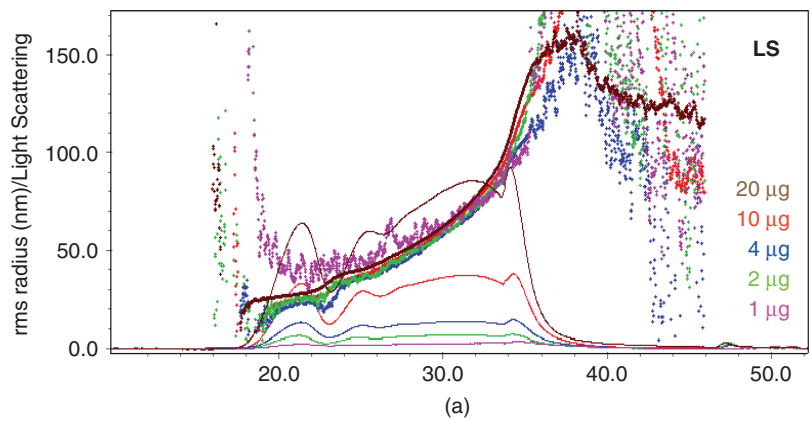
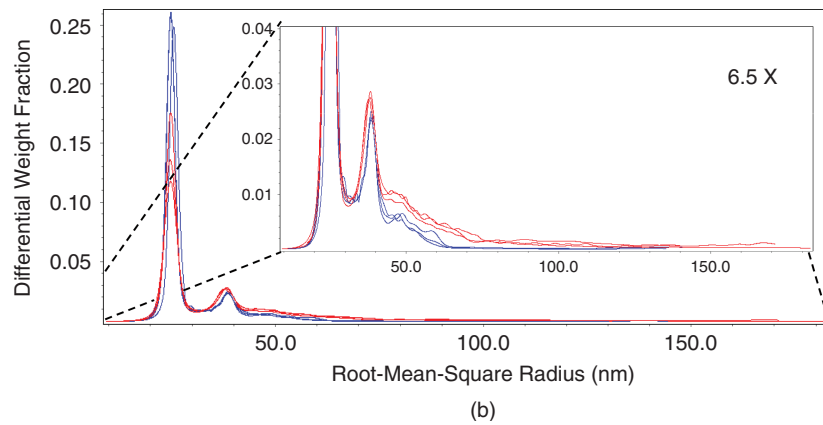
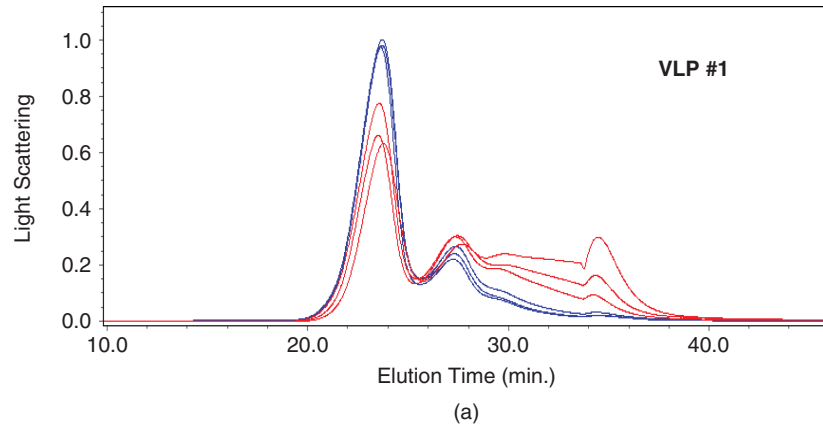
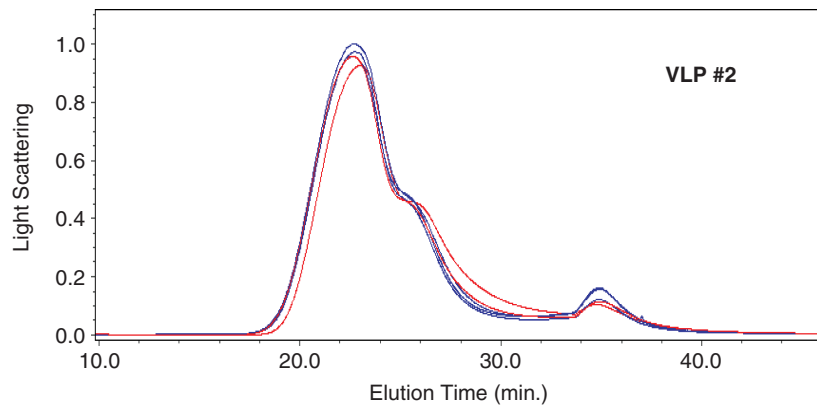


Figure 11.5. Effects of FFF mass load on signal-to-noise ratio in the calculated RMS data (a) and on sensitivity in UV absorbance detection (b).

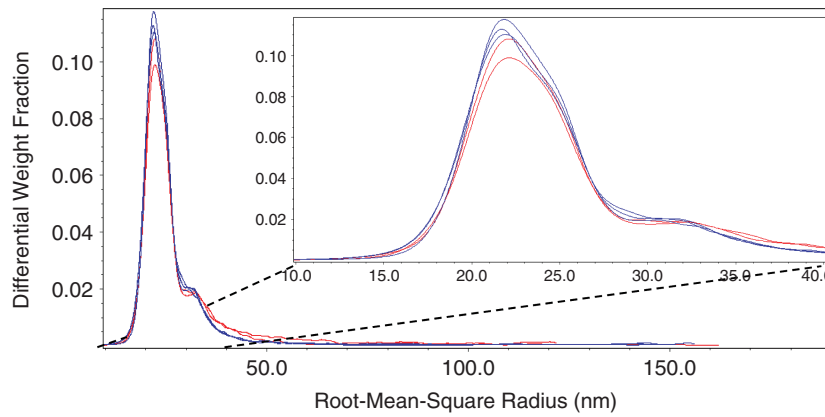


**Figure 11.6.** An overlay of (a)  $90^\circ$  light-scattering elution profiles for three early-stage-development lots (red traces) of VLP 1 and three later-stage-development preparations (blue traces); (b) calculated VLP size distribution profiles for each VLP preparation generated from the elution profiles in (a). Inset in (b) shows an expanded view of the  $y$  axis.





(a)



(b)

**Figure 11.7.** Overlay of (a)  $90^\circ$  light-scattering elution profiles for two very early-stage-development lots (red traces) of VLP 2 and three later-stage-development preparations (blue traces); (b) calculated VLP size distribution profiles for each VLP preparation generated from the elution profiles in (a). Inset in (b) shows an expanded view of the x axis to emphasize the overlap of two populations in the main peak.

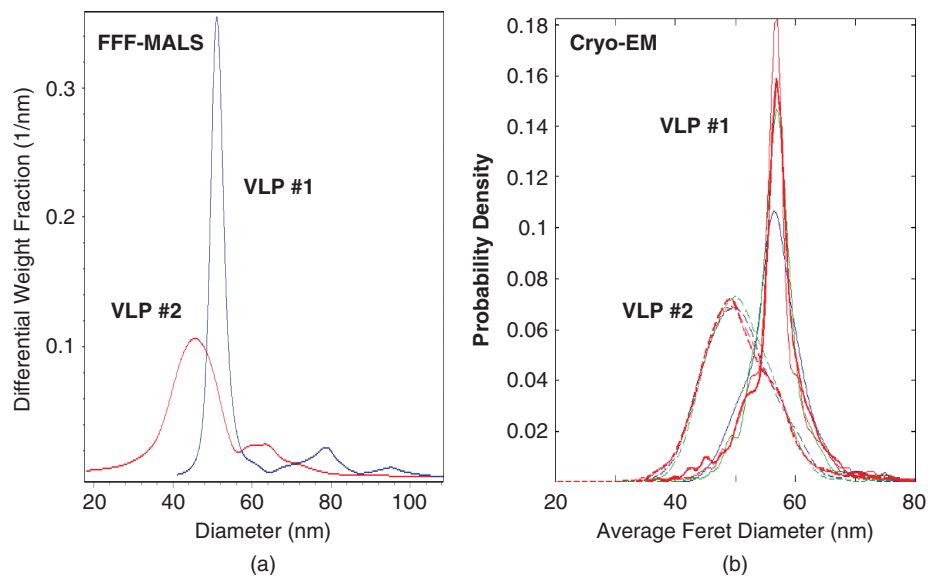


**Figure 11.8.** Comparison of size distribution profiles for VLPs 1 and 2 generated by FFF-MALS/UV (a) and Cryo-TEM [14] (b). Multiple traces in the cryo-TEM profiles for each VLP represent multiple analyses of the single preparation of each VLP.

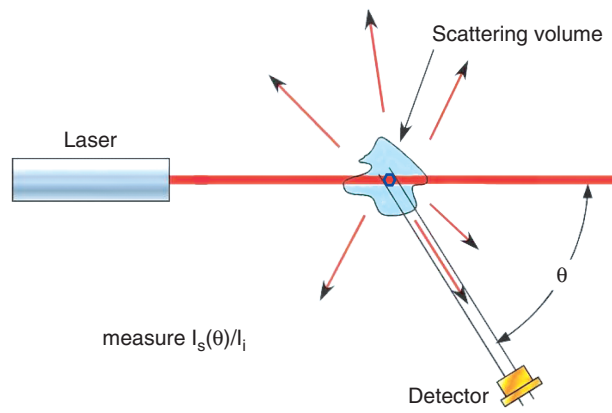
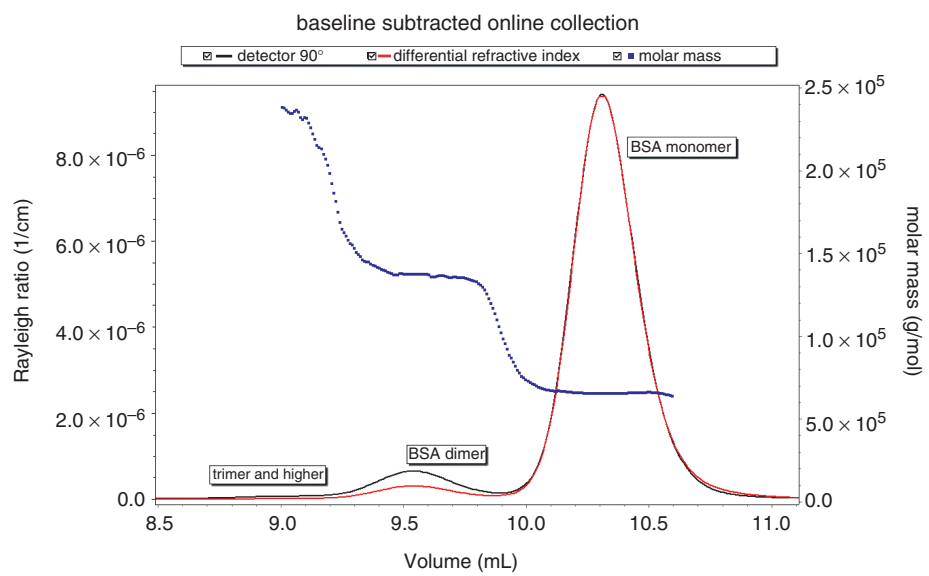
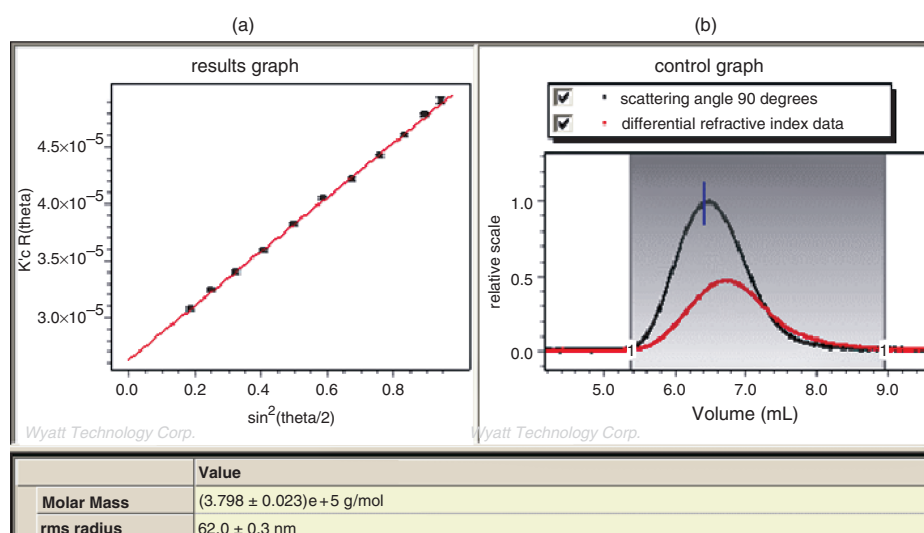


Figure 12.1. Detection of light scattered from a small volume of sample illuminated by a fine laser source beam.



**Figure 12.2.** Static light scattering (black trace) at 90° scattering, differential refractive index concentration detector (red trace), and molar mass (blue points) data as a function of elution volume for BSA fractionated via SEC.



**Figure 12.3.** Multiangle light scattering measurements for a sample fractionated via SEC: (a) the MALS data showing angular dependence of intensity, with inverse of the intensity versus  $\sin^2(\theta/2)$ , for the elution volume indicated by the vertical line in (b). Black points in (a) are data, and the line is a fit to the data with  $r_g = 62$  nm; (b) light-scattering signal (darker trace) at  $90^\circ$  scattering, and concentration detector signal (lighter trace) as a function of elution volume.

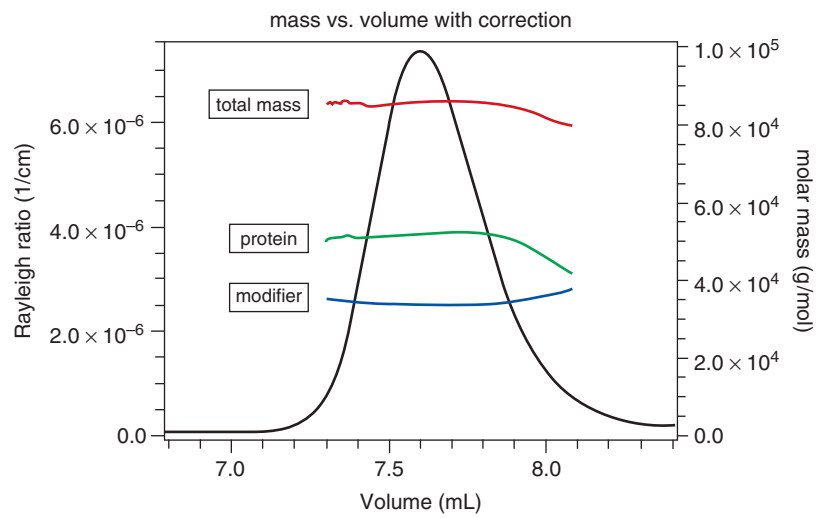


**Figure 12.4.** Multiangle conjugate analysis is used to determine the molar mass of protein, attached modifier, and the molar mass and radius of the complex.

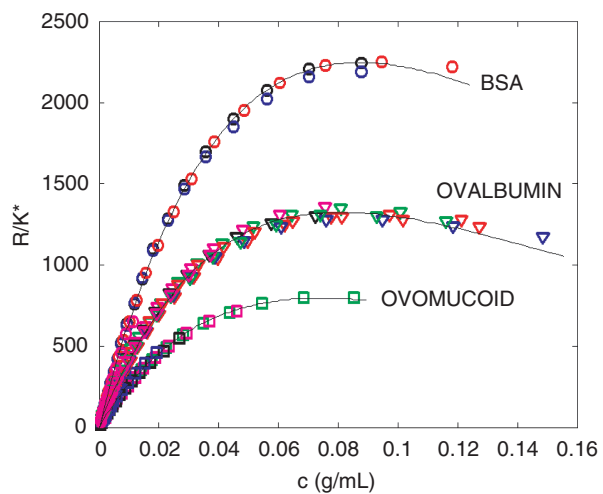


**Figure 12.5.** Multiangle LS data at  $90^\circ$  scattering taken as a function of concentration for BSA, ovalbumin, and ovomucoid. Points having different shades are data acquired during different experiments. The pronounced nonlinearity at higher concentrations arises from interactions. Solid lines are fits to a model of hard-sphere interactions. (Data from Fernandez and Minton [19].)

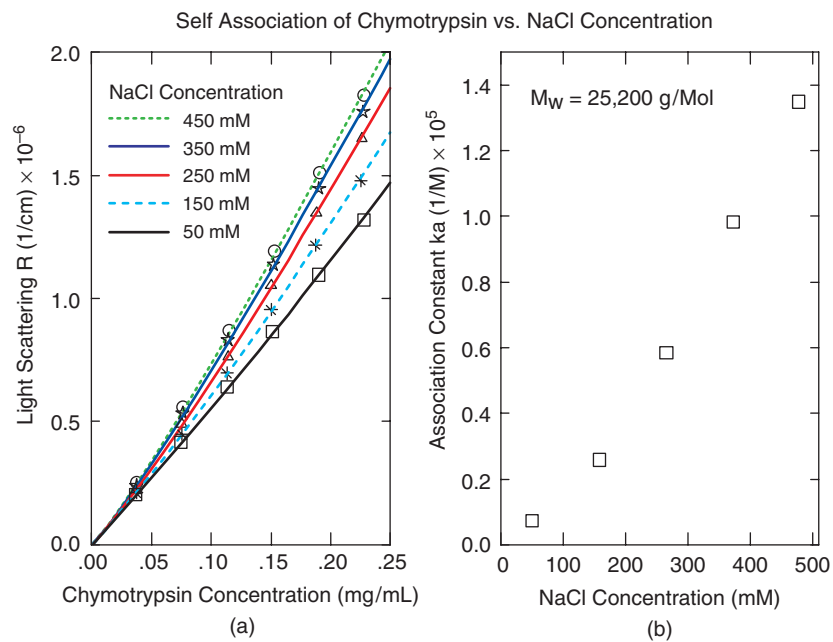
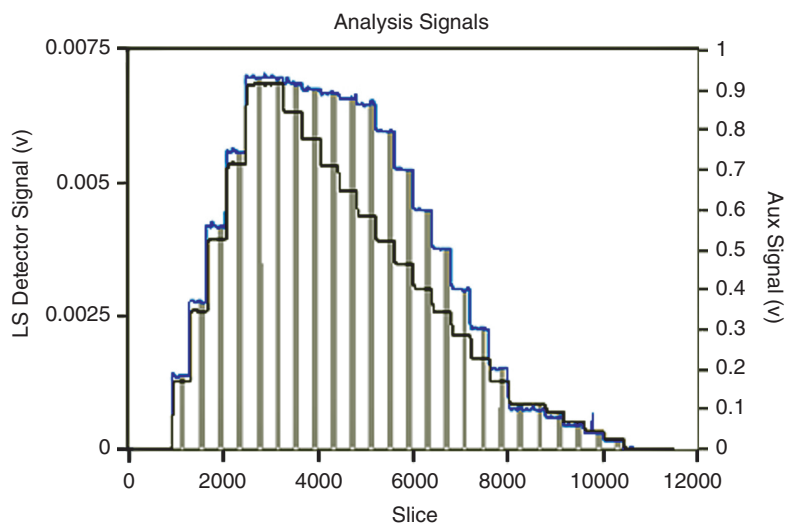
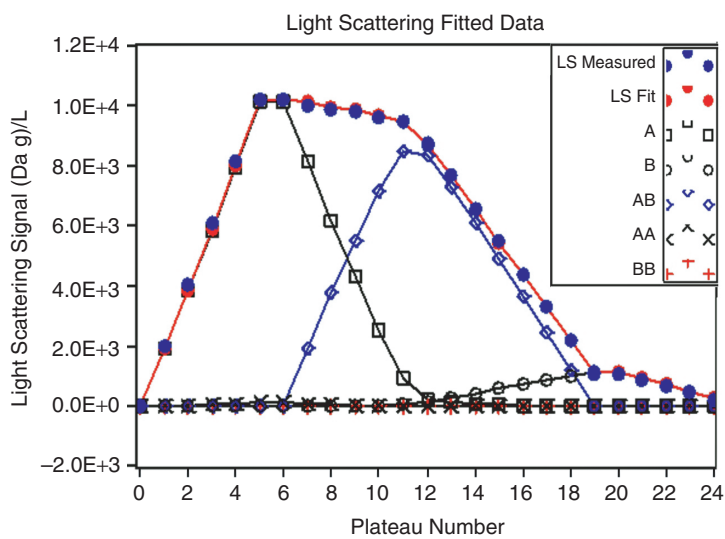


**Figure 12.6.** Multiangle LS free-solution self-association measurements of chymotrypsin: (a) MALS data as a function of chymotrypsin concentration for different NaCl concentrations; solid lines are fits to the model of Eq. (12.6); (b) the resulting association constants  $k_a$  for the different NaCl concentrations. (Unpublished data of Hanlon and Some [25].)





(a)



(b)

**Figure 12.7.** Multiangle LS free-solution self- and heteroassociation measurements of chymotrypsin and bovine pancreatic trypsin inhibitor (BPTI): (a) MALS data (upper trace) and concentration detector data the MALS trace is significantly above the concentration detector trace during the crossover from 100% chymotrypsin to 100% BPTI due to associations. In (b) MALS data (solid circles) derived from (a), along with the results of a fit (line through solid circles) to a model of self- and heteroassociation.

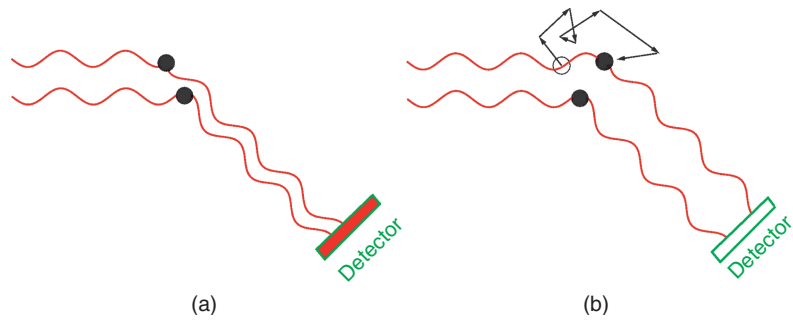


**Figure 12.8.** (a) Two particles have a spatial relation resulting in constructive interference of scattered light at the detector; (b) the particles have moved with respect to one another, causing the scattered light to interfere destructively at the detector. Thus, the intensity viewed by the detector varies through time.

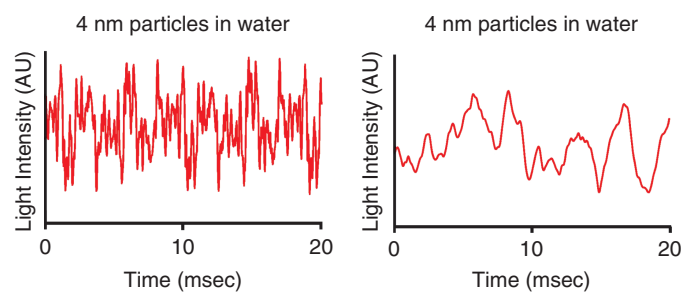


**Figure 12.9.** (a) Intensity of light through time expected for 4-nm-radius particles diffusing in water; (b) intensity through time expected for 40-nm radius particles.

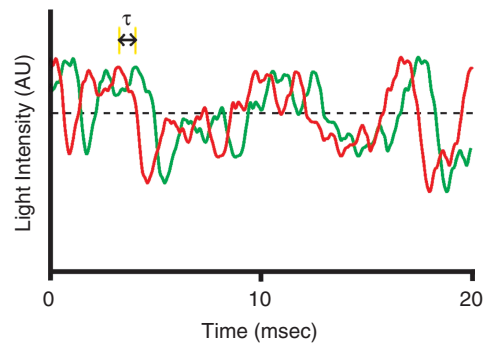


**Figure 12.10.** Simulated data of intensity through time, overlaid with the same intensity through time, offset in time by delay time  $\tau$ . The intensity through time is correlated to itself at short delay times, but becomes uncorrelated to itself at long delay times.

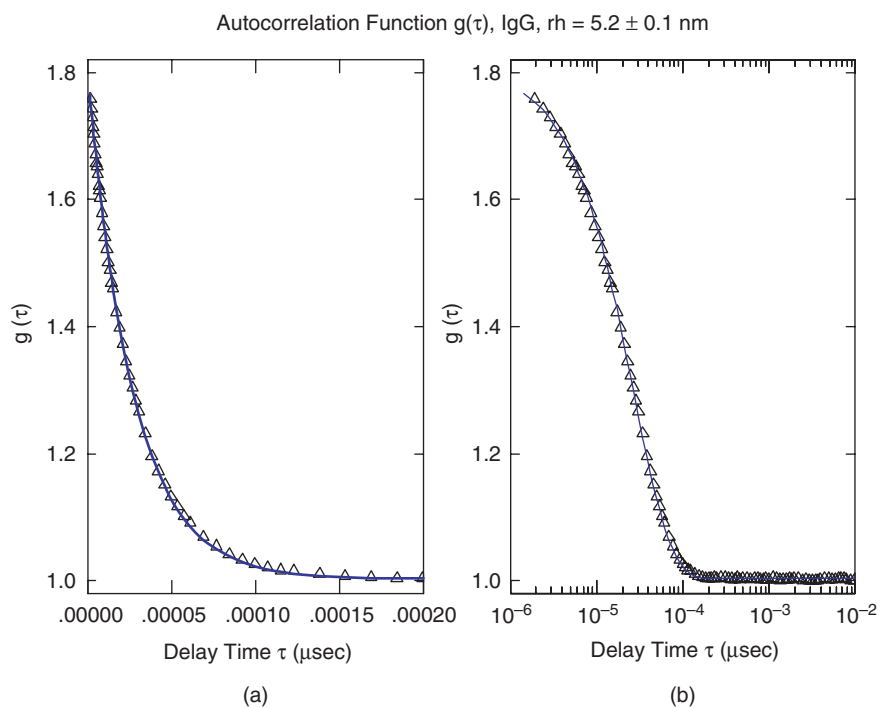


**Figure 12.11.** (a) Autocorrelation Function data (triangles) along with a fit of the data to a simple exponential function (line); (b) the same data and fit displayed with a log time axis. A log time axis is used in order to simultaneously view many time regions. Data are for an IgG sample and are taken online in flow mode, after SEC separation.

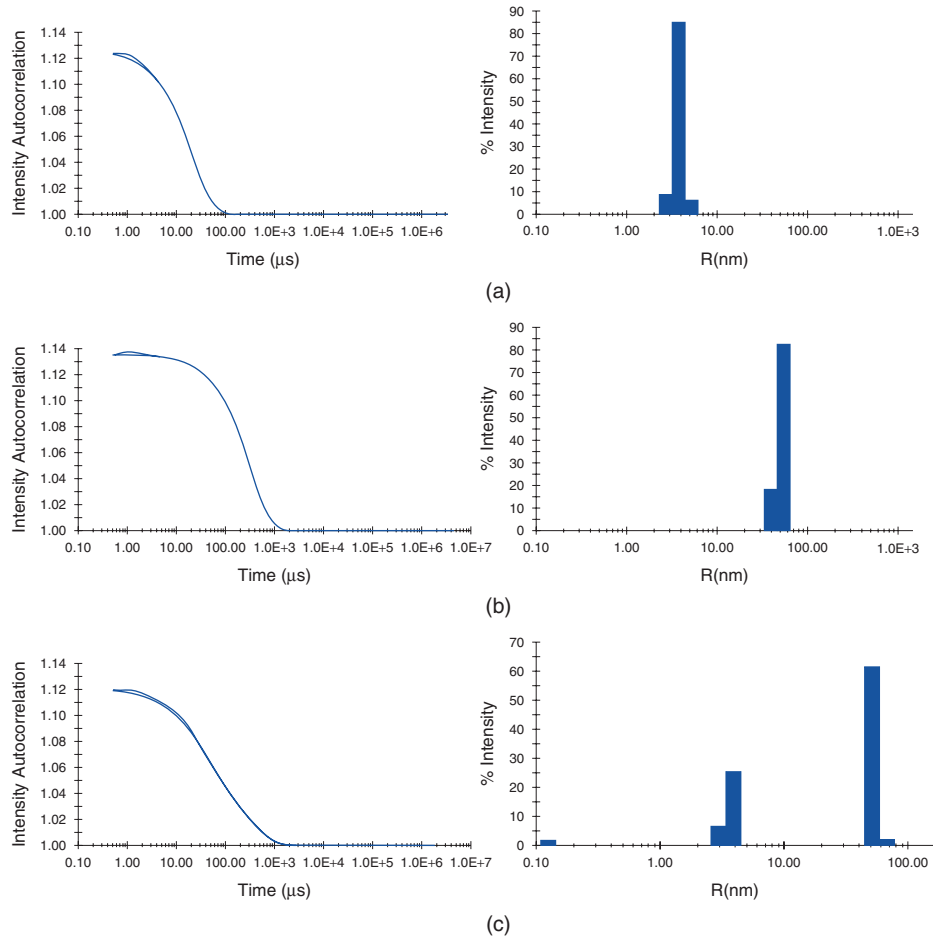


**Figure 12.12.** Data and regularization fits for three samples. Data for (a) and (b) are from two different monodisperse species, and data for (c) is from a mixture of the two.

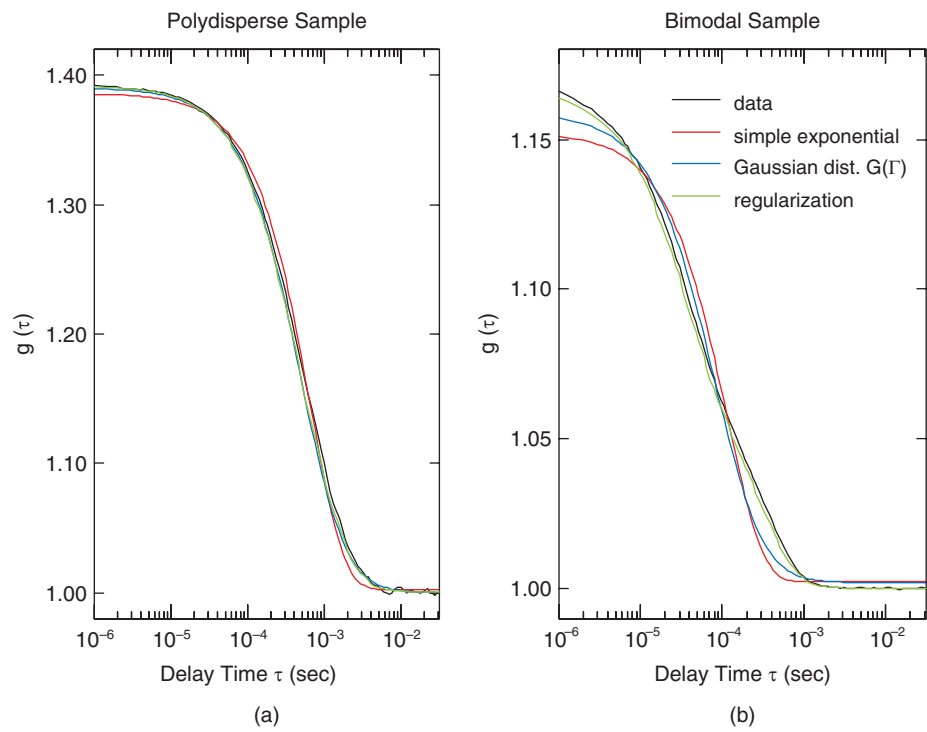
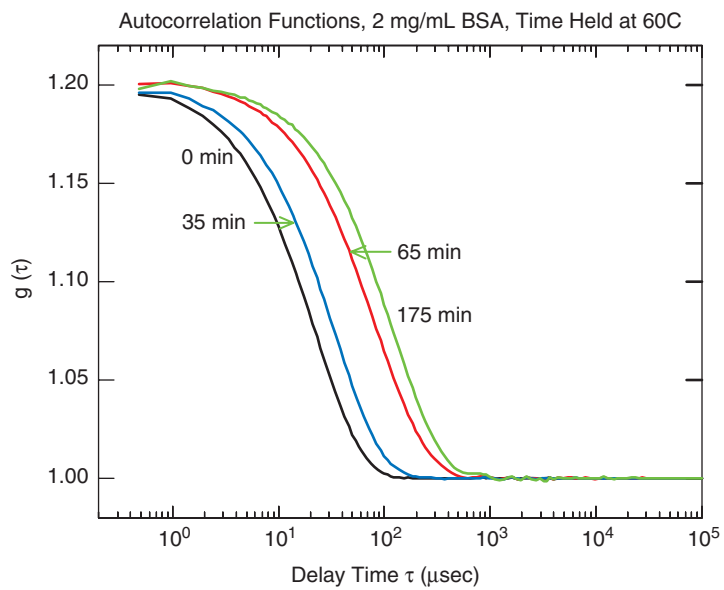
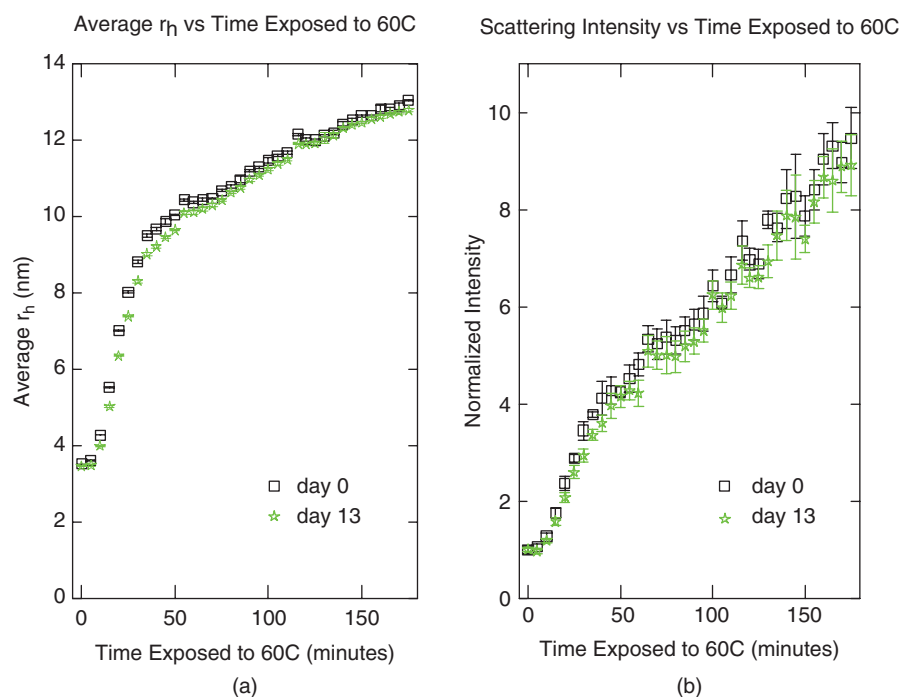


Figure 12.13. (a) Data and fits to a polydisperse sample; (b) data and fits to a sample prepared for a bimodal distribution (mix of  $r_h = 3.8$  nm and  $r_h = 50$  nm). Both 5- $\mu$ L samples were measured within a 1536-well plate, using a Wyatt DynaPro DLS plate reader.



**Figure 12.14.** Autocorrelation functions for 2 mg/mL BSA aliquots exposed to 60°C for 0, 35, 65, and 175 min.





**Figure 12.15.** Measurements of 36 aliquots, all measurements made at 5°C, all samples stored at 4°C–5°C: (a) the average hydrodynamic radius as a function of time that the aliquot was exposed to 60°C; (b) the intensity of scattered light, which is proportional to the weight averaged molar mass, as a function of time that the sample was exposed to 60°C. The intensity data were normalized to the intensity of the time 0 sample.

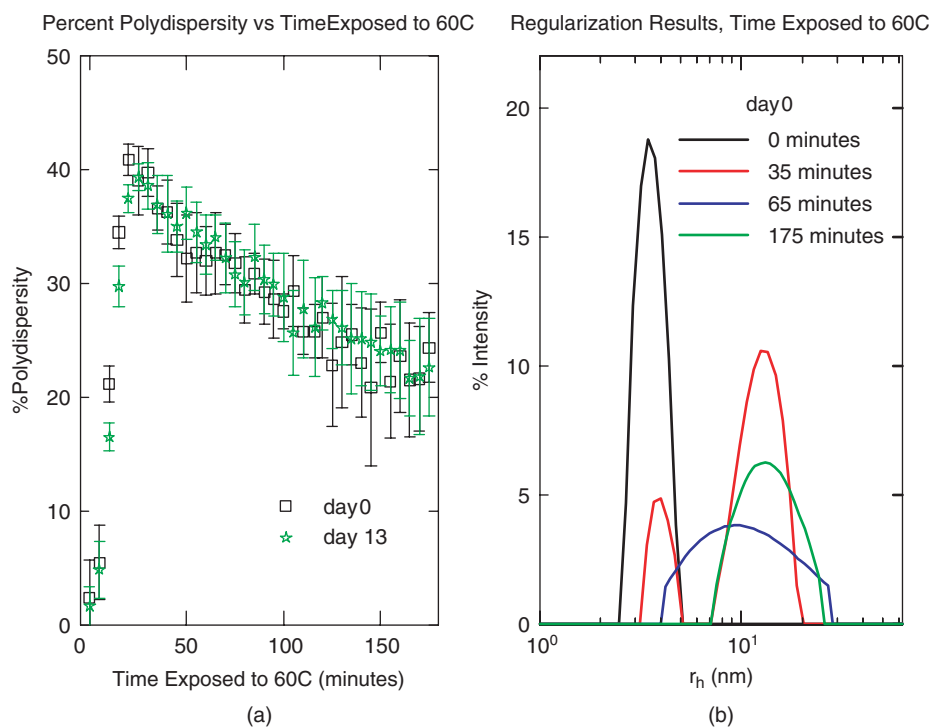


**Figure 12.16.** All measurements made at 5°C, all samples stored at 4°C–5°C: (a) sample polydispersity as a function of time sample is exposed to 60°C, as measured on days 0 and 13; (b) results of regularization analysis, where the actual distributions of sizes present in the samples are estimated, for samples exposed to 60°C for 0, 35, 65, and 175 mins.

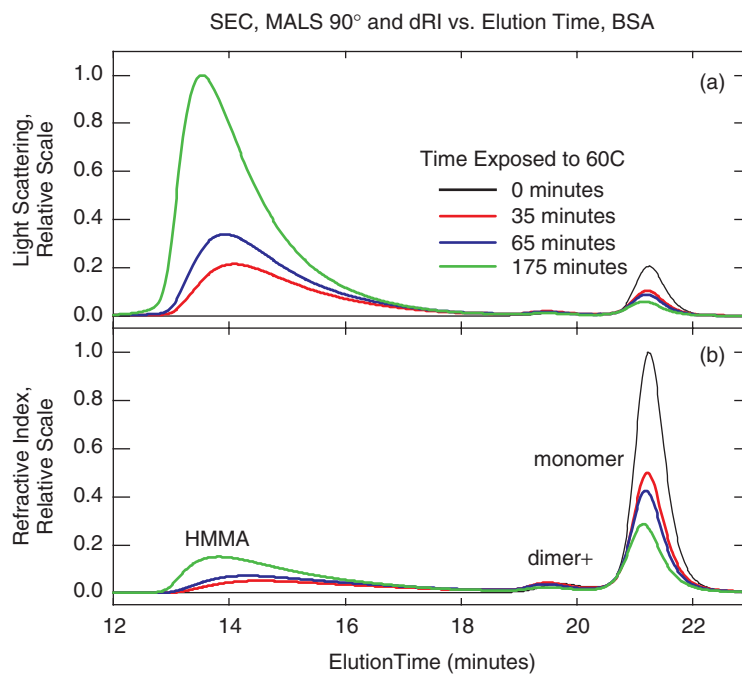


**Figure 12.17.** (a) Multiangle LS 90° light scattering; (b) differential refractive index concentration data for BSA exposed to 60°C for different periods of time, and fractionated via SEC. The contrast between the MALS and the concentration detector traces clarifies the molar mass difference between the different species present in the samples.

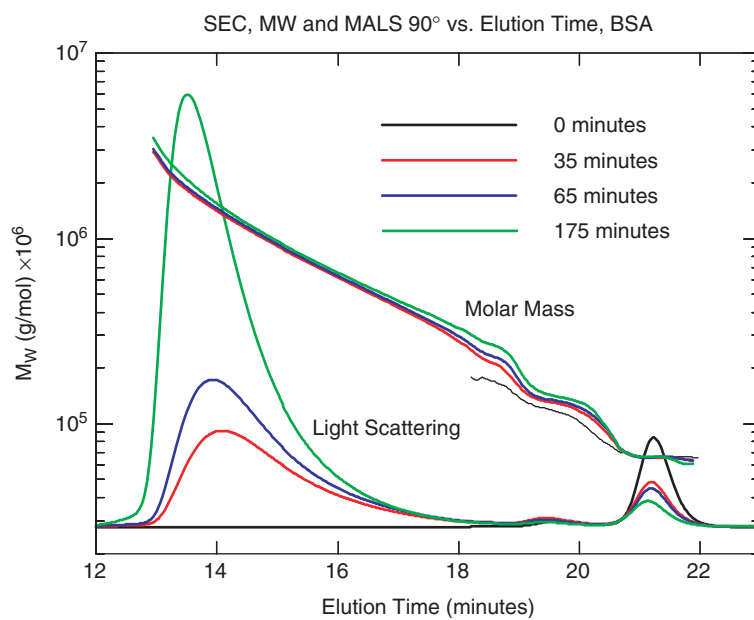


**Figure 12.18.** Multiangle LS 90° light scattering and molar mass results derived from both the MALS and the concentration detectors for BSA exposed to 60°C for different periods of time.

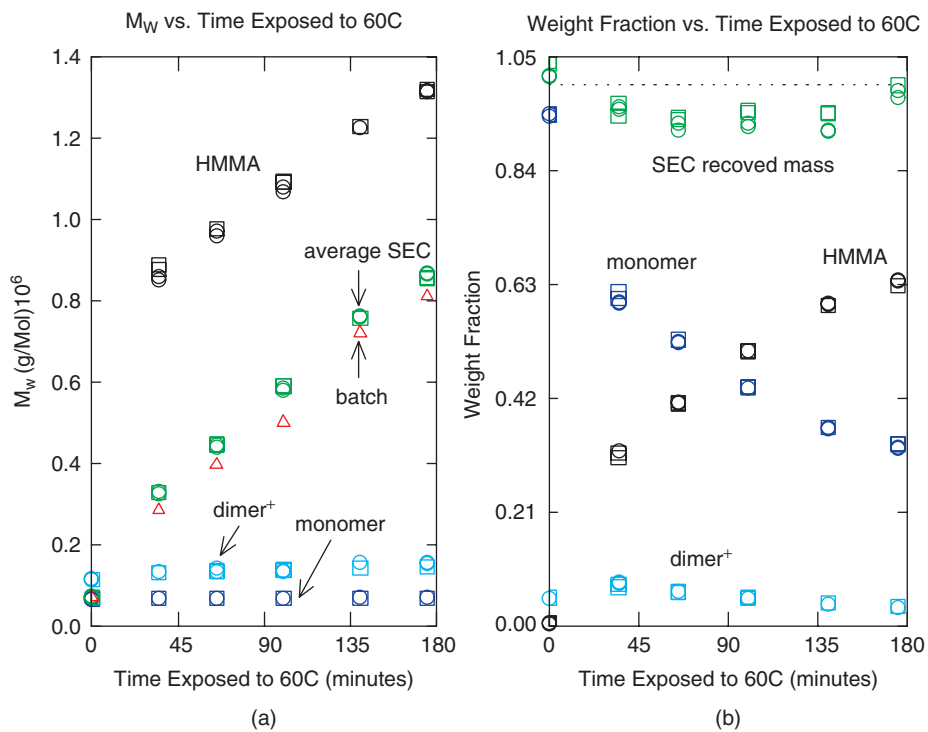
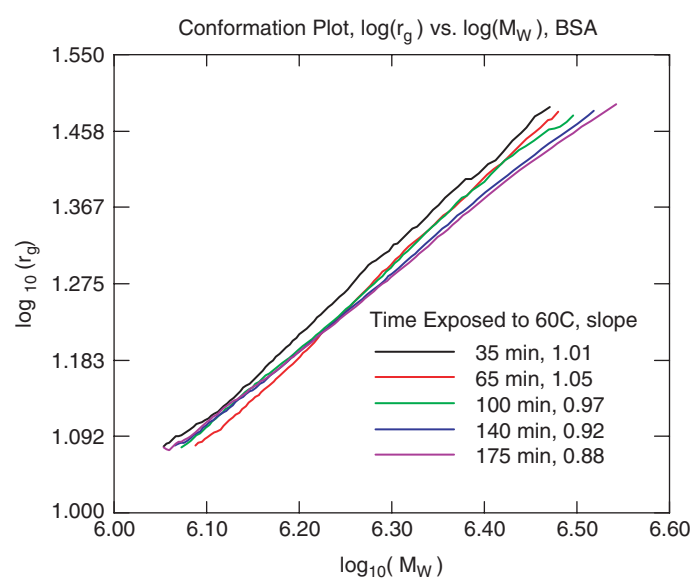
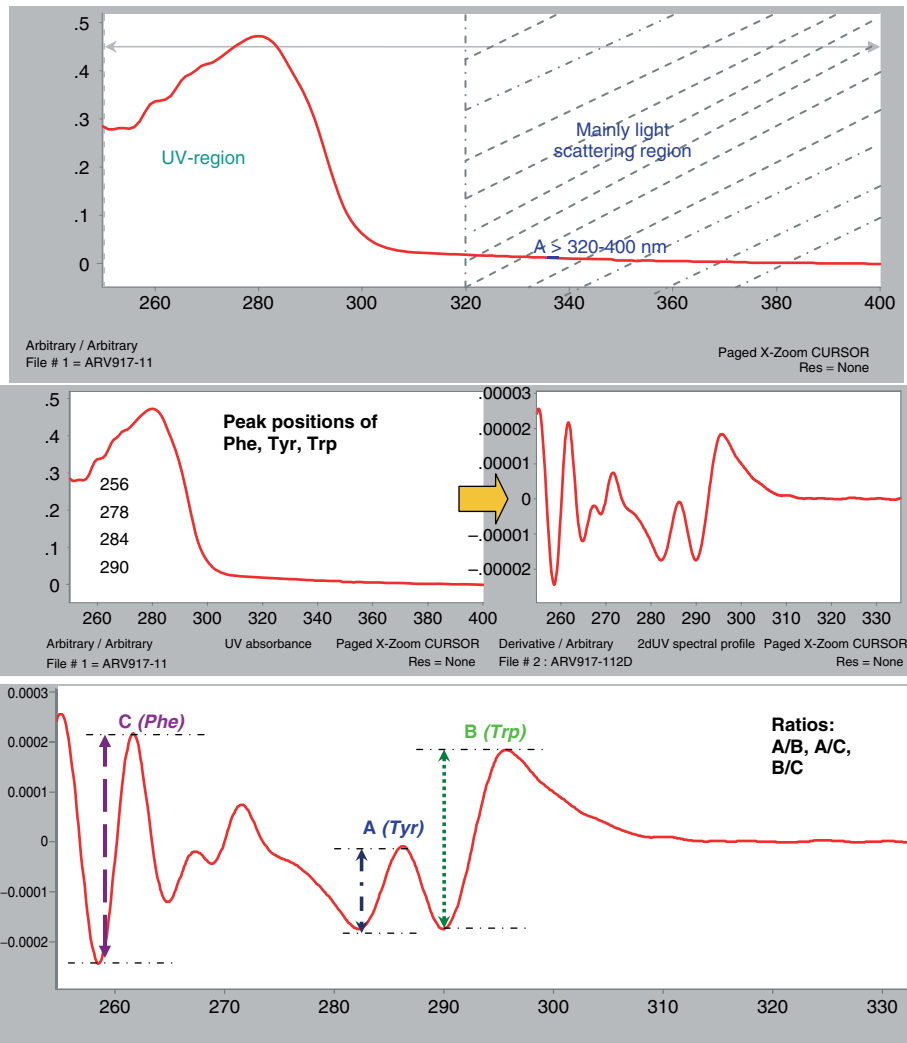


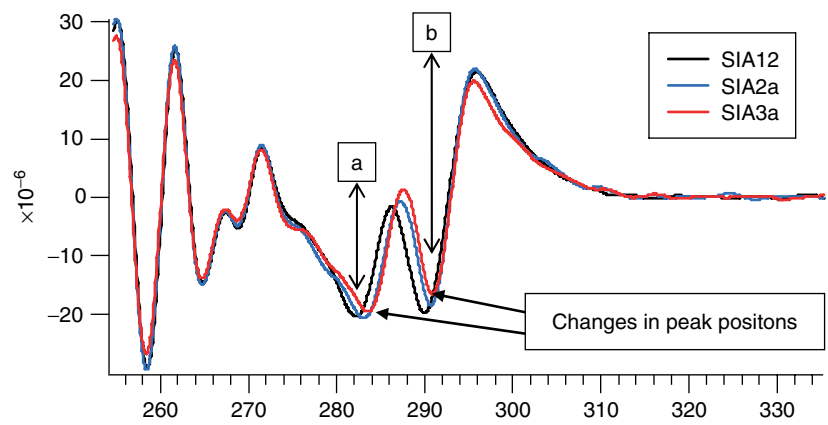
Figure 12.19. (a) Multiangle LS results for batch measurements and for duplicate SEC measurements at two concentrations. Squares indicate SEC data for 2 mg/mL concentration, circles indicate SEC data for 0.33 mg/mL concentration, and triangles indicate batch measurements at 0.4 mg/mL. Shown are the weight-averaged molar masses for (1) each peak in SEC as described in the text, (2) all SEC peaks in combination, and (3) batch measurements. Panel (b) shows concentration detector data for the weight fractions of each peak, and the percent SEC recovered mass.



**Figure 12.20.** Conformation plot from HMMA species. The slope of the resulting line is equal to  $1/a$ , where  $a$  is the power of the radius by which the mass increases. For solid spheres  $a = 0.33$ , for ideal random coils under theta conditions  $a = 0.5$ , and for rods  $a = 1.0$ .



**Figure 13.2.** Use of UV-visible spectroscopy of a protein to obtain protein quantitation, protein aggregation, and tertiary conformational analysis by second derivative.



	a/b ratio	IU/mL
SIA 12 = 10 mg/ml untreated control	0.454	38.9
SIA 2a = 65 min/50°C	0.496	18.8
SIA 3a = 120 min/50°C	0.573	10.2

**Figure 13.3.** Correlations between tertiary conformational changes and protein activity. Significant changes are observed in both peak ratios ( $a/b$ ), peak positions, and protein activity [in international units per milliliter (IU/mL)].



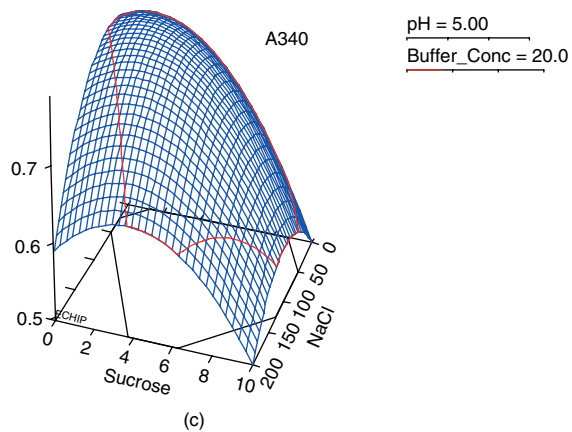
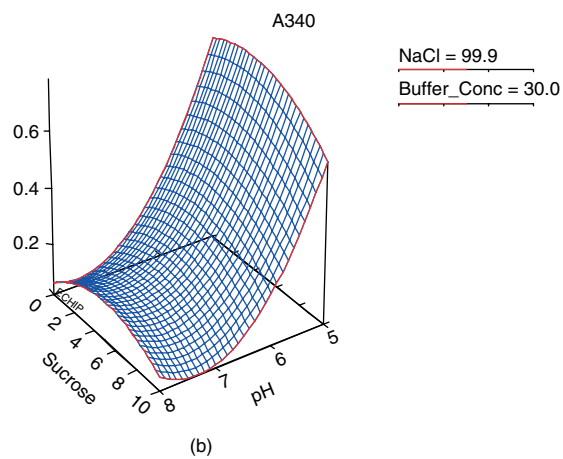
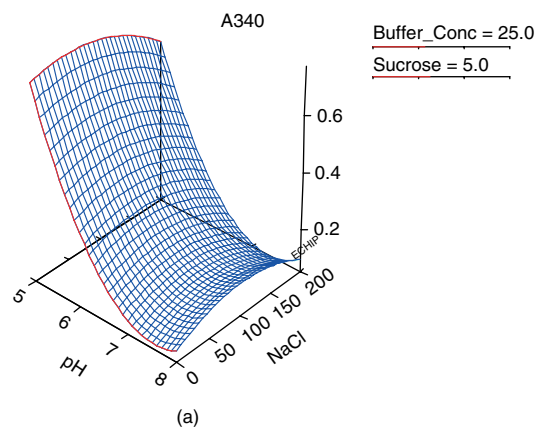


Figure 13.5. Response surface plots of A340 as a function of pH, sucrose, and NaCl.

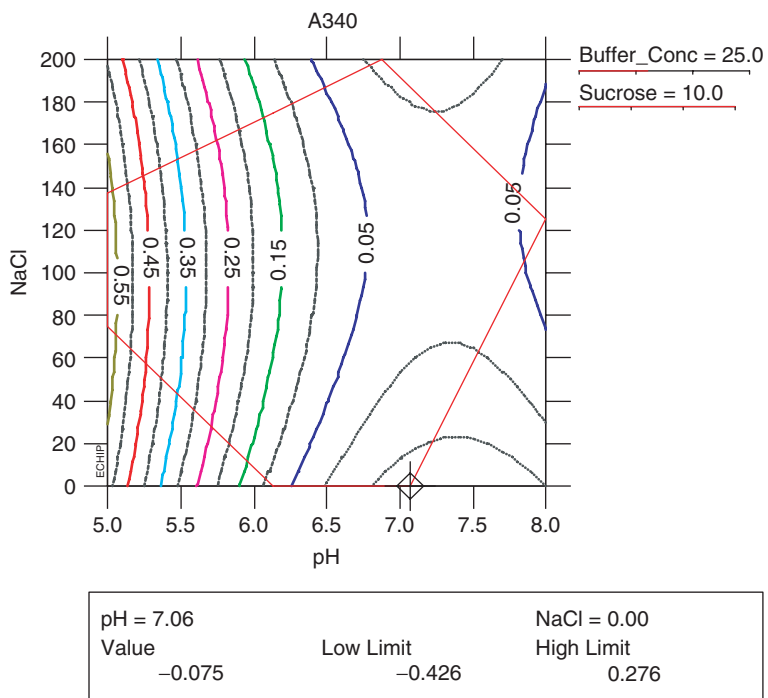
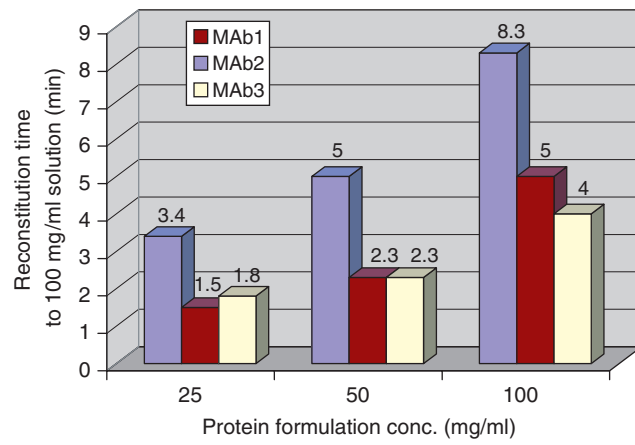
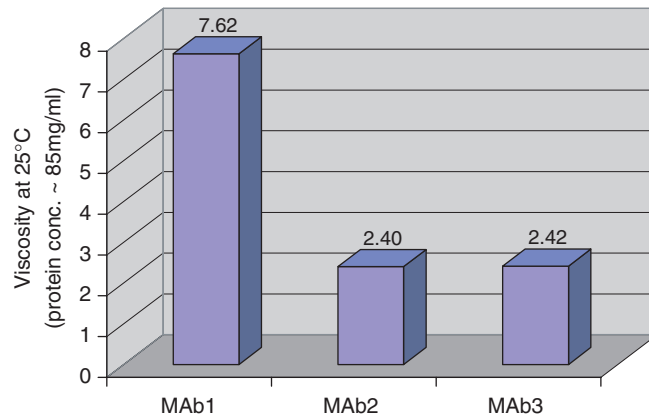


Figure 13.6. Optimal isotonic formulation of ovalbumin as predicted by the response surface formulation model.

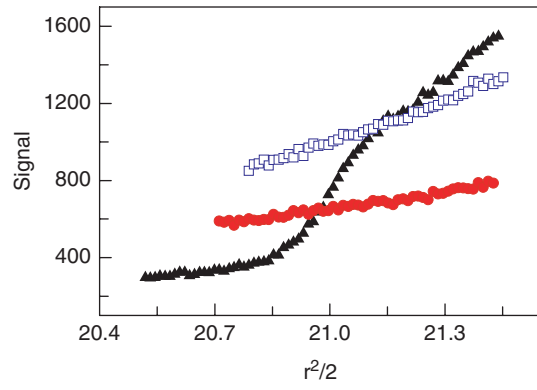


(a)

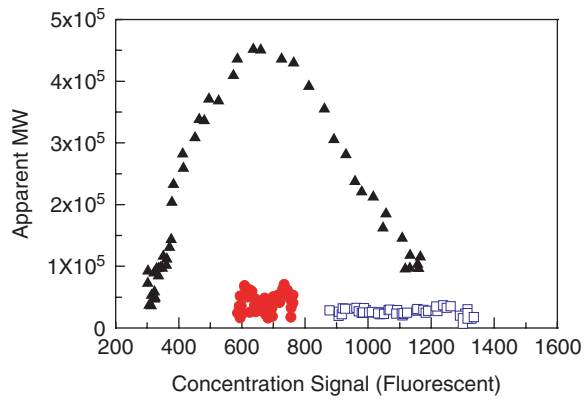


(b)

**Figure 15.1.** Three humanized IgG1 MAbs with the same IgG1 human Fc construct but different complementarity-determining regions (CDRs) formulated identically and lyophilized using the same lyophilization process: (a) time to reconstitute the lyophilized cake resulting in a final MAb concentration of 100 mg/mL; (b) viscosity at 25°C after reconstitution to a final MAb concentration of 85 mg/mL.

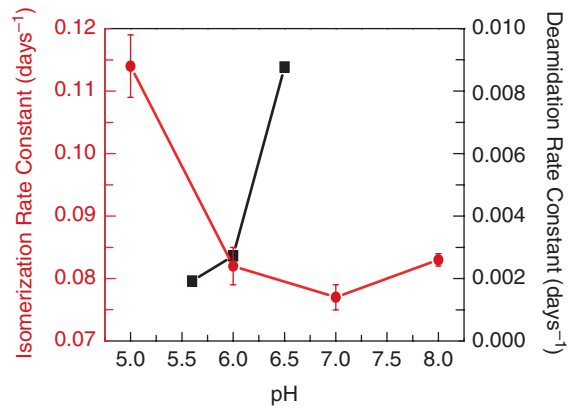


(a)

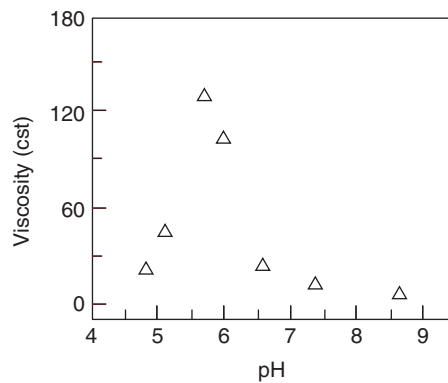


(b)

**Figure 15.2.** Sedimentation equilibrium of the same three MAbs as in Figure 15.1. The data were collected using the fluorescence detection system in a Beckman-AVIV XLF analytical ultracentrifuge. The MAbs were fluorescently labeled [59], characterized to ensure integrity, and added to unlabeled high-concentration solution to serve as a tracer for detection. (a) The raw fluorescence signal data as a function of radial position; (b) apparent molecular weight determined from the data in panel (a).



(a)



(b)

Figure 15.4. Humanized IgG1 MAb1 formulated at 100 mg/mL: (a) isomerization rate constant for an Asp residue and deamidation rate constant for an Asn residue as a function of pH; (b) kinematic viscosity as function of pH.

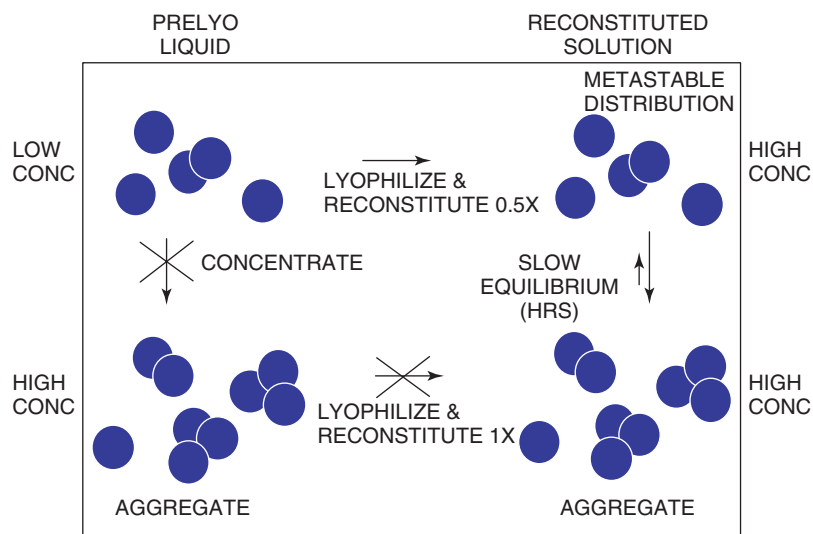


**Figure 16.5.** High-concentration lyophilized formulation strategy for proteins susceptible to aggregation. This strategy involves processing the protein at low concentration at 0.5× excipient levels, and then reconstituting the lyophilized cakes to half the original fill volume. (Unpublished data.)

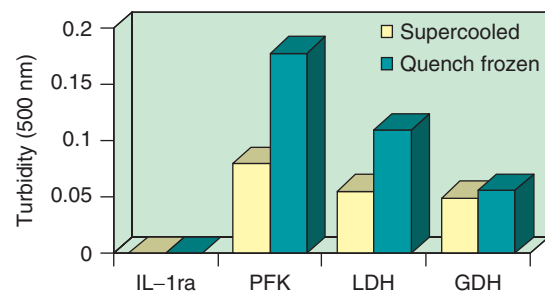
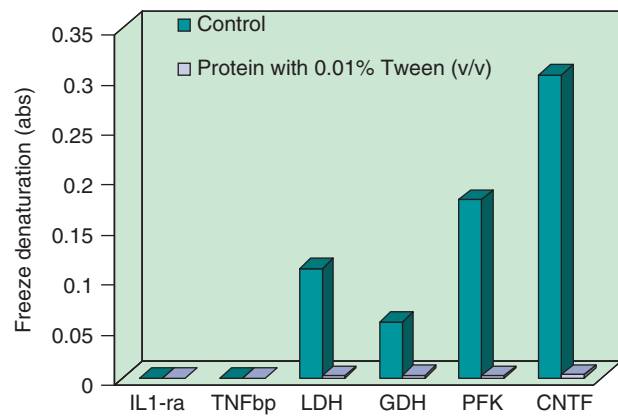
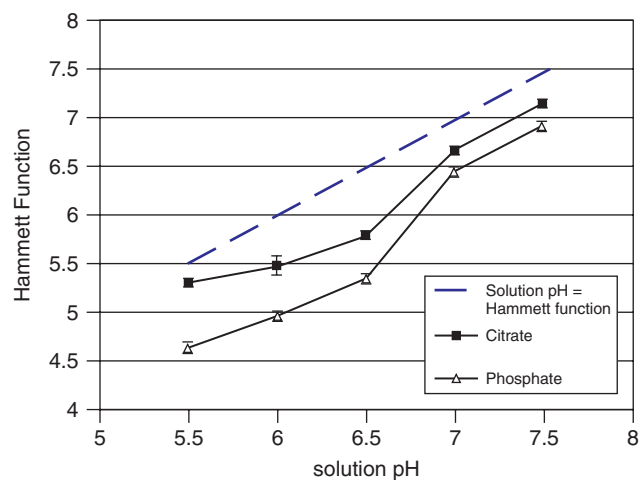


Figure 18.1. Effect of freezing rate on protein precipitation during freezing. (Courtesy Byeong Chang.)



**Figure 18.2.** Effect of polysorbate on protein stability during freezing. (Courtesy Byeong Chang.)





**Figure 20.1.** Hammett acidity functions of lyophilized trehalose/buffer formulations as a function of prelyophilization solution pH of citrate (■) and phosphate (△) buffered systems. The bold dashed line indicates a hypothetical situation in which the Hammett functions are numerically equal to the prelyophilization solution pH. The other two lines are shown as visual aid. (The figure was prepared using data reported by Chatterjee [50].)

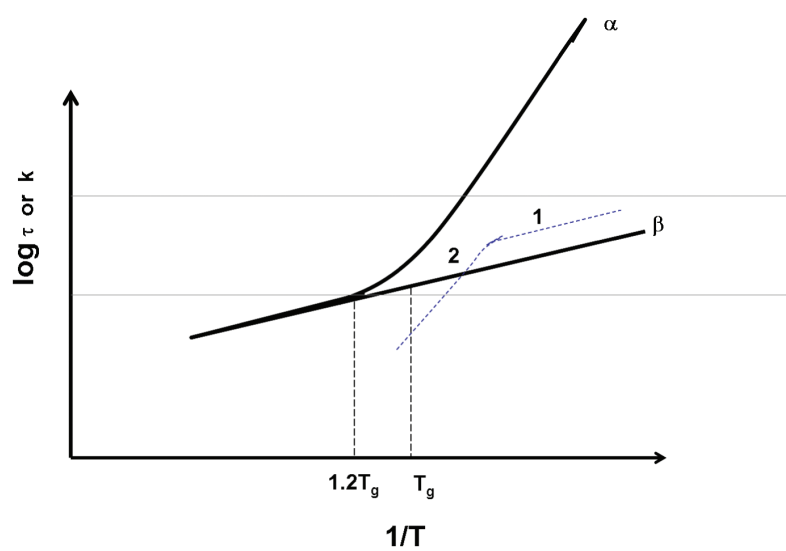


**Figure 21.8.** Schematic of  $\alpha$  and  $\beta$  motions as a function of temperature. (The dashed-line curve) shows the degradation reaction rate; segment 1 represents the temperature window when reactivity is correlated with  $\beta$  mobility; segment 2 shows the temperature window when reactivity is correlated with  $\alpha$  mobility [90].

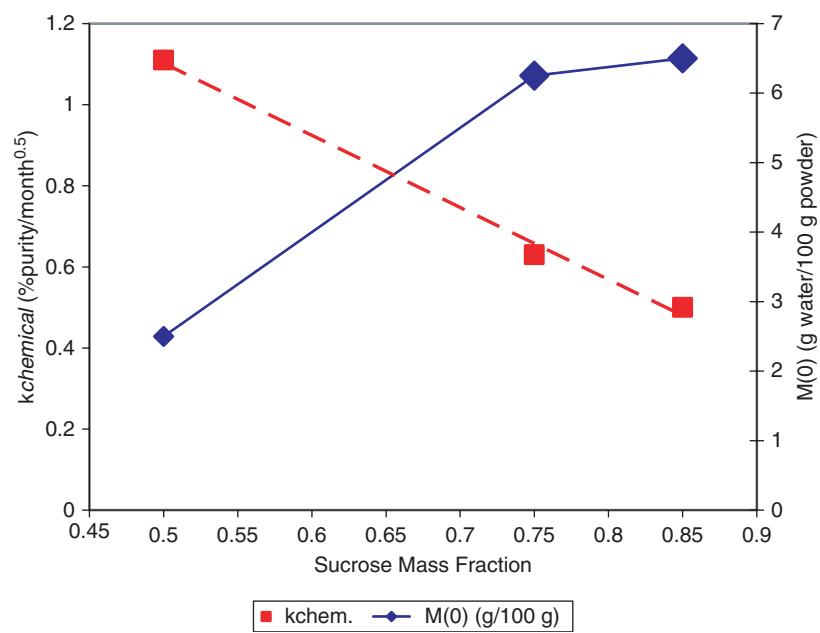
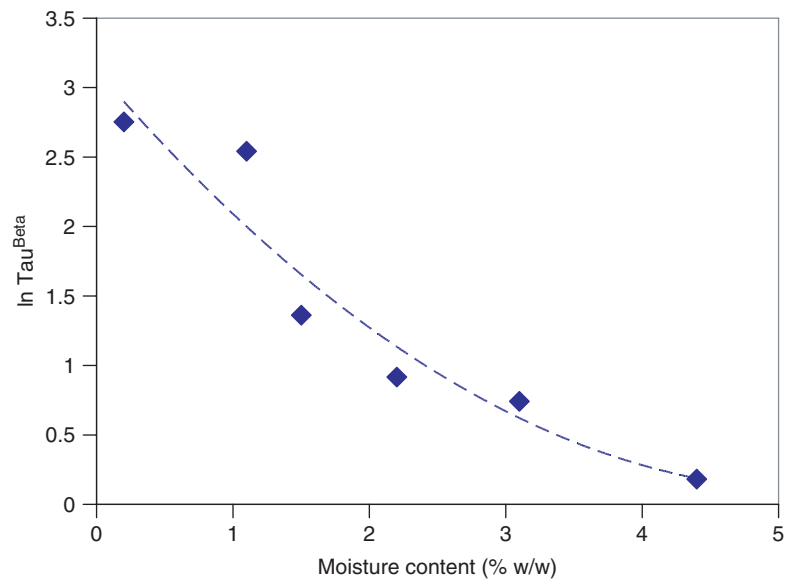


Figure 23.2. Correlation between chemical stability of hGH and  $M_0$  in freeze-dried formulations with different fractions of sucrose. (Figure constructed from data in Constantino et al. [26] and Pikal et al. [29].)



**Figure 23.3.** Relationship between molecular mobility and moisture content in a representative IgG<sub>1</sub> formulations. (Figure constructed from data in Chang et al. [16].)

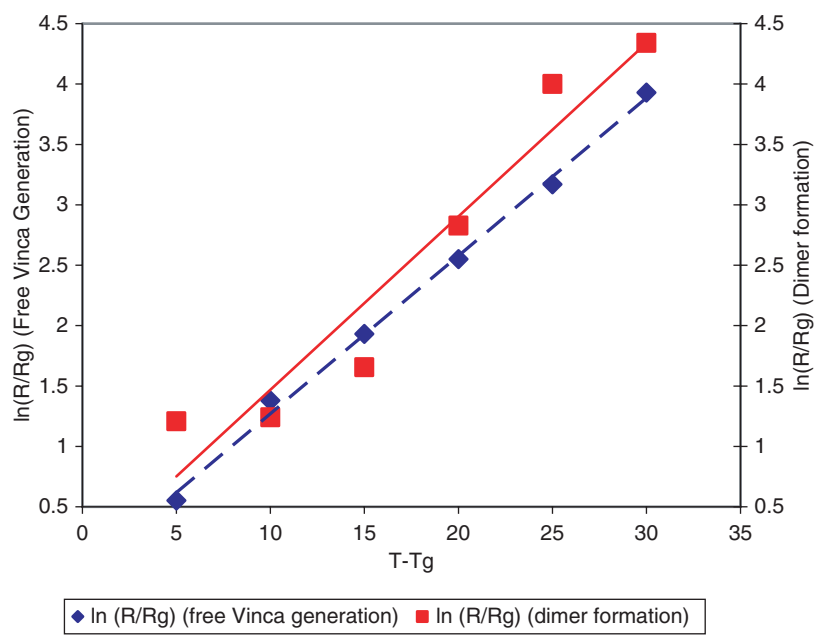


Figure 23.4. Relationship between chemical degradation and  $T - T_g$  in a Vinca alkaloid antibody. (Figure constructed from data in Roy et al. [40].)

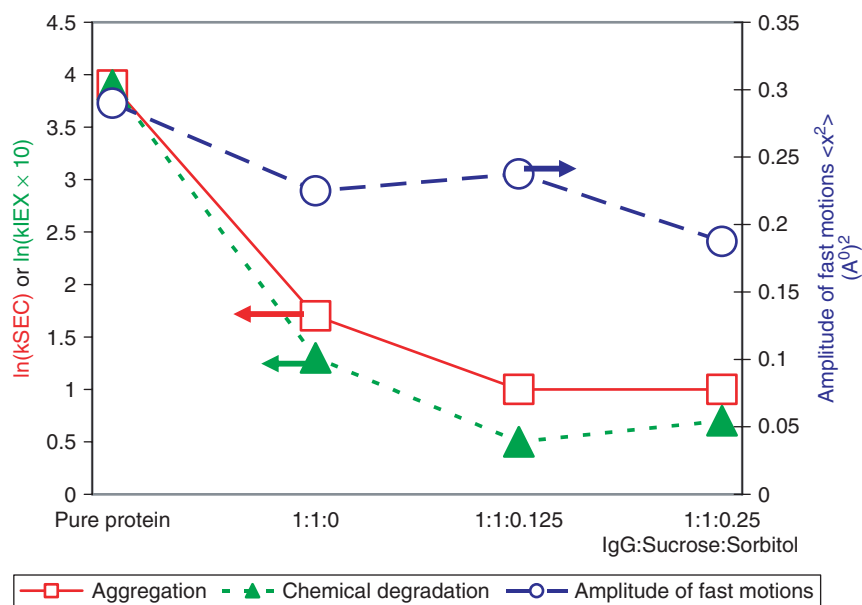


Figure 23.5. Relationship between fast dynamics and storage stability (chemical and physical) of different freeze-dried formulations of IgG<sub>1</sub>. (Figure constructed from data in Cicerone et al. [35].)

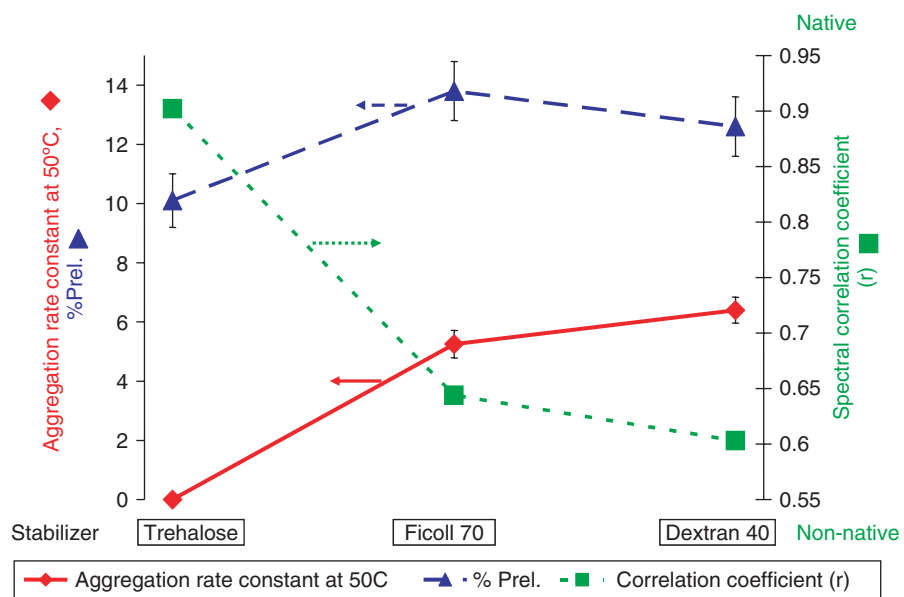
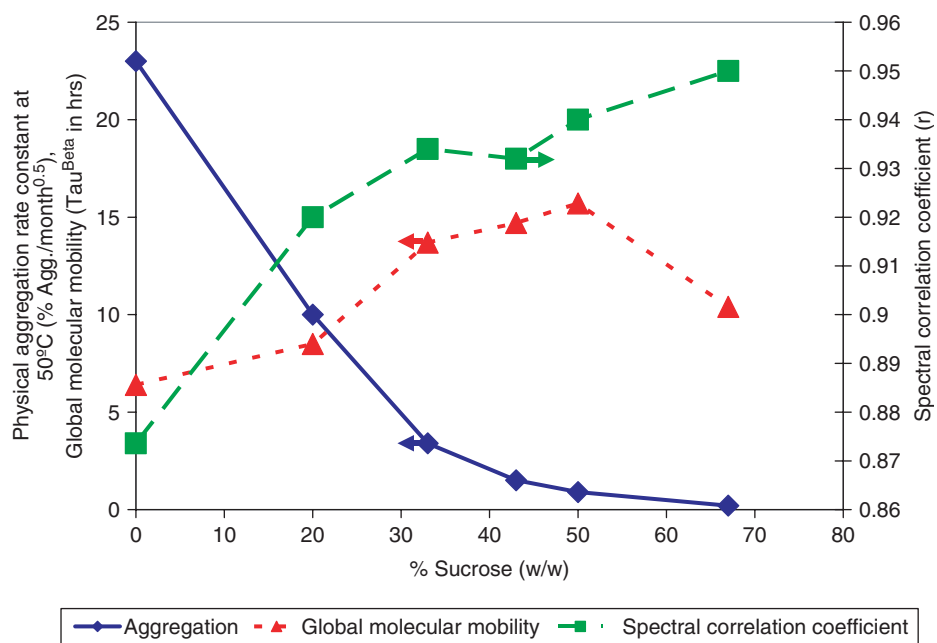
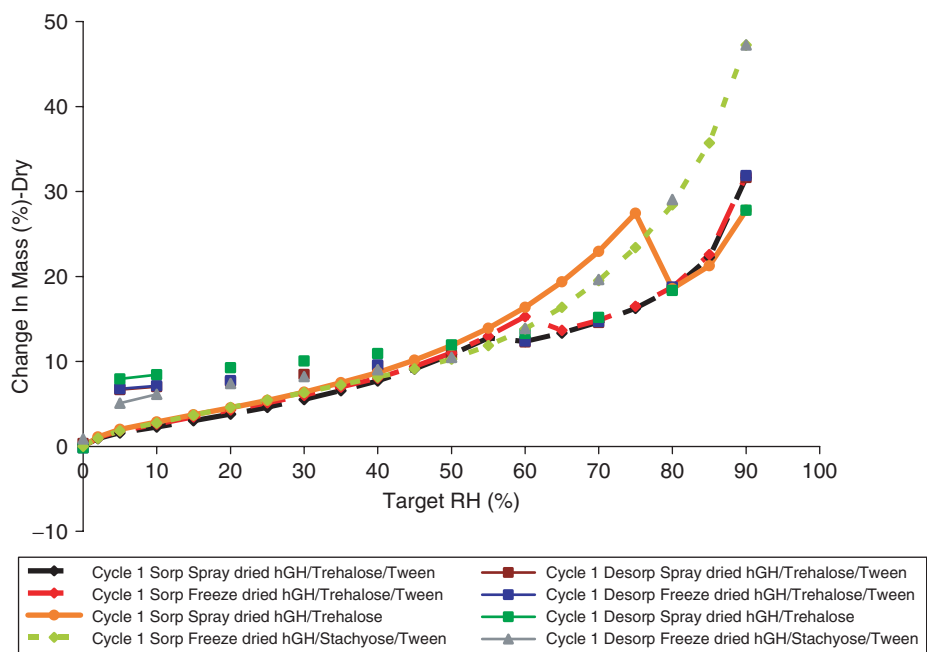


Figure 23.6. Relationship between protein secondary structure, protein surface accumulation, and physical stability of Met-hGH in different freeze-dried formulations. (Figure constructed from data in Abdul-Fatah et al. [20].)



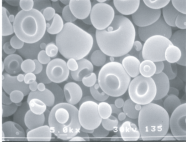


**Figure 23.7.** Relationship between protein secondary structure, global molecular mobility, and physical stability of an IgG<sub>1</sub> in different freeze-dried formulations. (Figure constructed from data in Chang et al. [14].)





**Figure 23.8.** Differences between moisture sorption isotherms of spray-dried and freeze-dried formulations of hGH in trehalose or stachyose matrices with or without surfactant (Tween) [53], Abdul-Fattah et al., unpublished data.

			
	Foam	Lyo cake	Spray dry powder
Specific surface area:	0.06–0.09 m <sup>2</sup> /g	0.6–0.8 m <sup>2</sup> /g	2.6–3.1 m <sup>2</sup> /g
Best case stability (Vaccine stored at 37°C)	4.2 months	0.6 months	0.4 months

\* 27 months time point, data shown for live B/Harbin Influenza virus vaccine

**Figure 23.10.** Different drying methods applied to the same formulation resulted in different solid-state structures and properties [57] Truong et al., unpublished data.

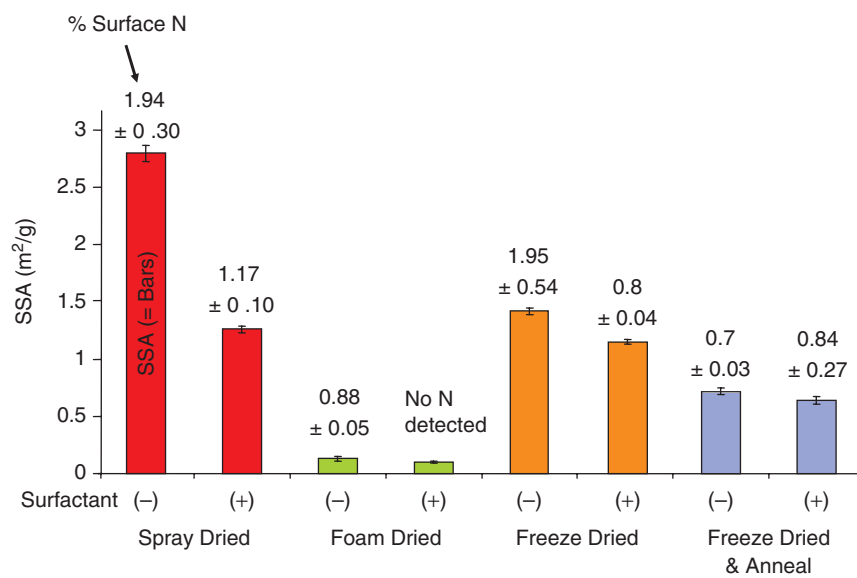


**Figure 23.11.** Surface heterogeneity of two formulations for a vaccine of PIV3 virus dried by different methods (colored bars represent specific surface area, while values above colored bars represent percentage of surface N (Nitrogen) as measured by ESCA). (Figure constructed from data in Abdul-Fatah et al. [59].)

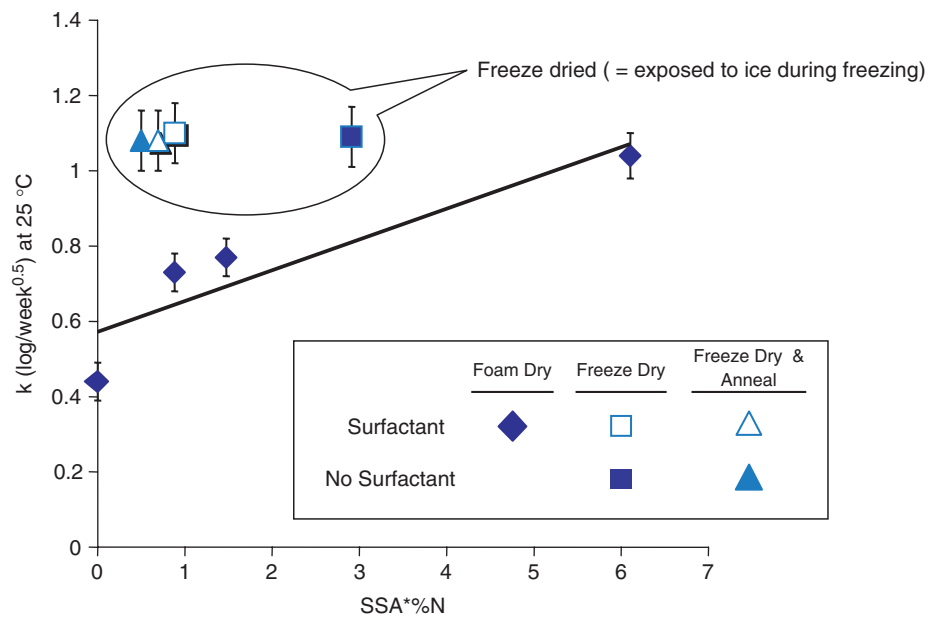


**Figure 23.12.** Relevance of specific surface area and surface composition to PIV3 vaccine stability at 25°C. A similar trend was observed at 37°C. (Figure constructed from data in Abdul-Fatah et al. [59].)

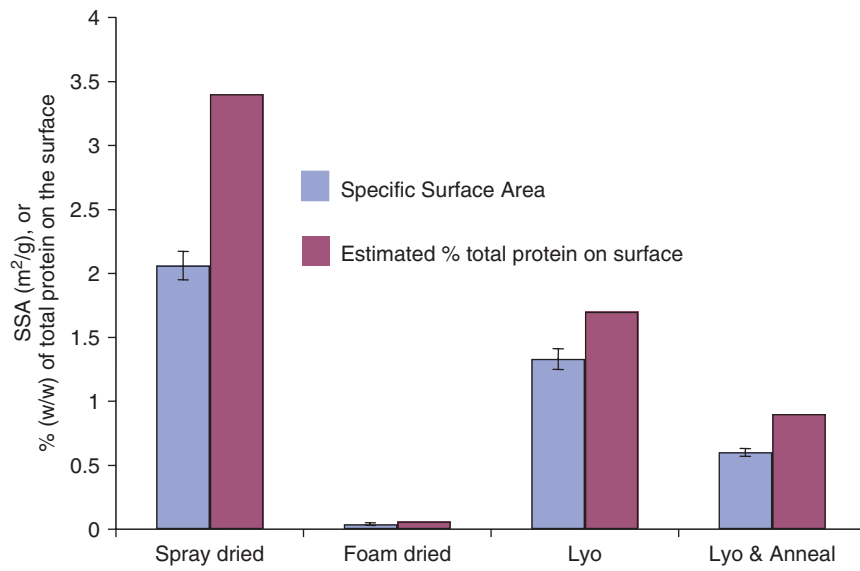


Figure 23.13. Specific surface area (SSA) and surface composition in a 1:4 system of IgG1:sucrose. (Figure constructed from data in Abdul-Fatah et al. [60].)

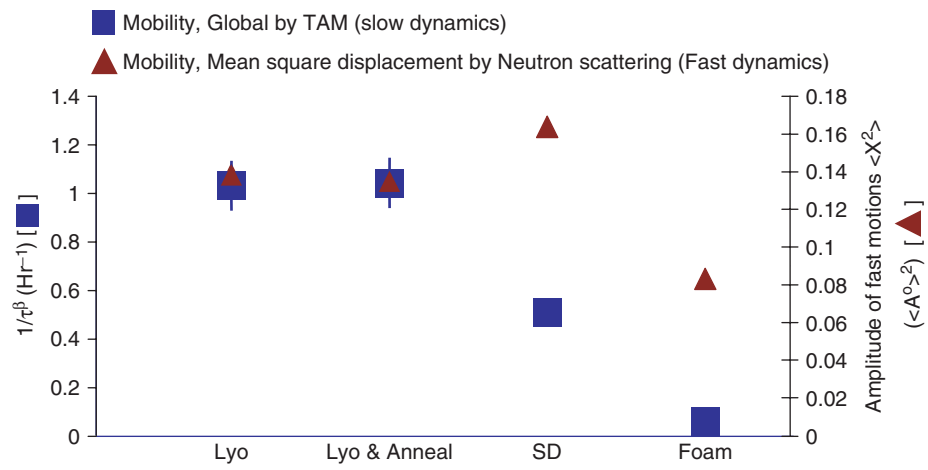
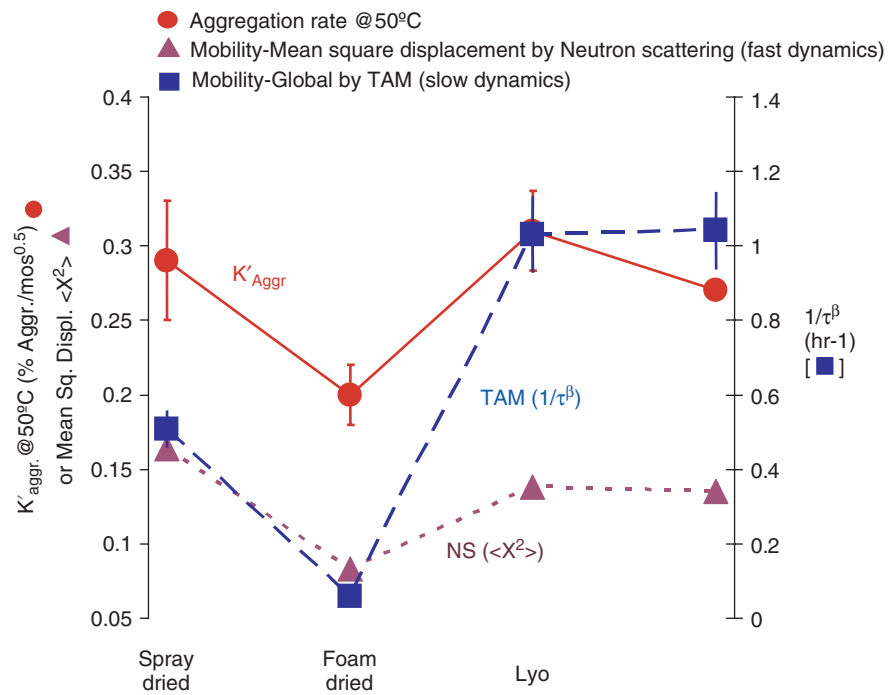


Figure 23.14. Molecular mobility at 50°C in a 1:4 system of IgG1:sucrose. (Figure constructed from data in Abdul-Fatah et al. [60].)



**Figure 23.15.** Correlation of storage stability at 50°C to molecular mobility in a 1:4 system of IgG1:sucrose. (Figure constructed from data in Abdul-Fatah et al. [60].)

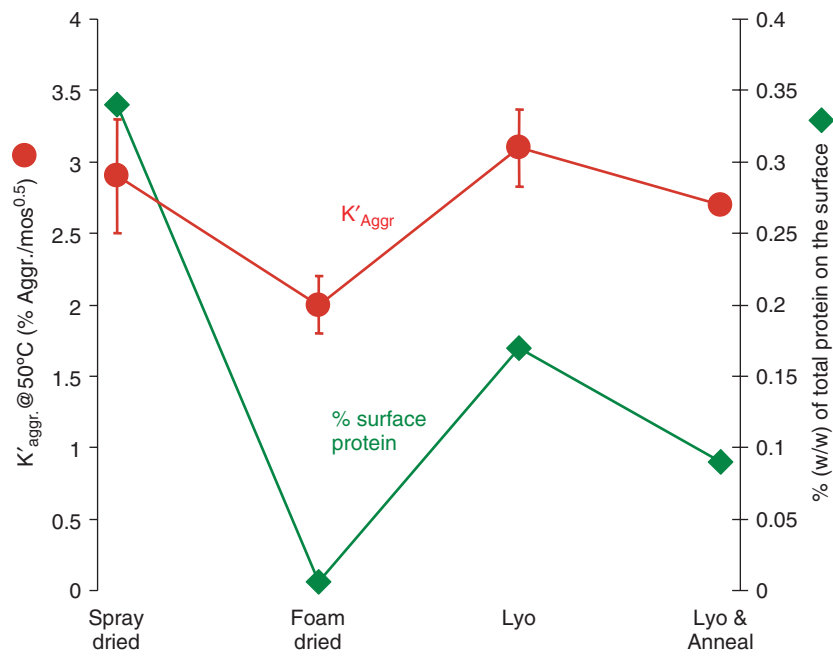


Figure 23.16. Correlation of storage stability at 50°C to surface composition in a 1:4 system of IgG1:sucrose. (Figure constructed from data in Abdul-Fatah et al. [60].)



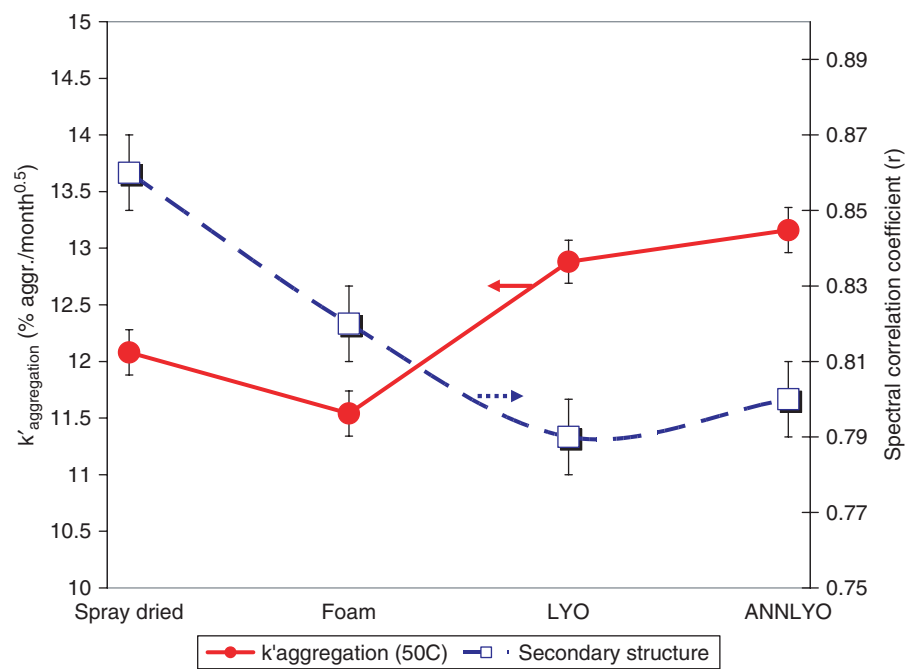
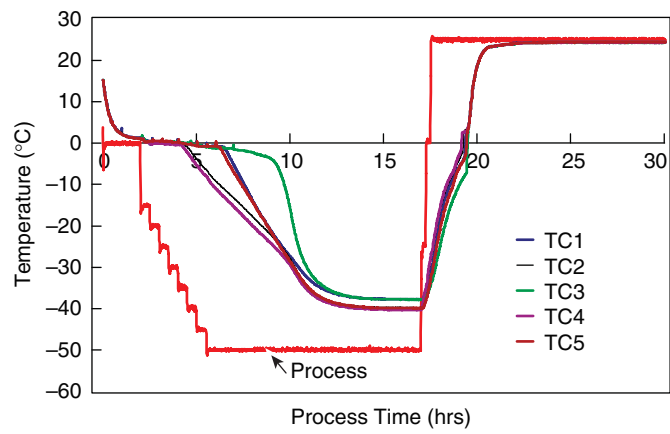


Figure 23.17. Correlation of storage stability at 50°C to protein secondary structure in a 4:1 system of IgG1:sucrose. (Figure constructed from data in Abdul-Fatah et al. [60].)



**Figure 26.12.** Illustrative freeze-thaw profile in a cryowedge. Thermocouples are placed at different positions in the wedge. The “process” probe represents the temperature of the heat transfer fluid.

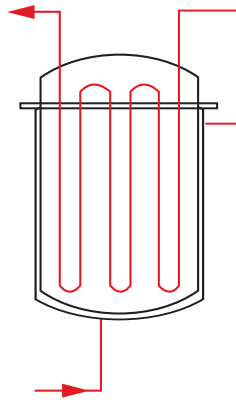
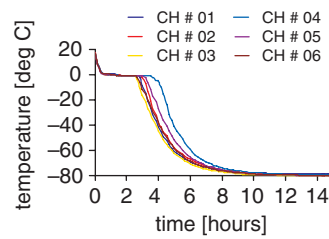
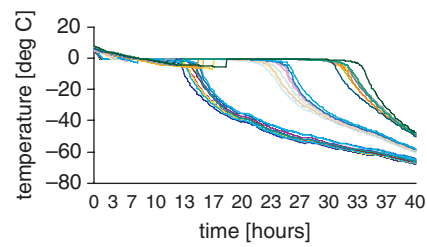
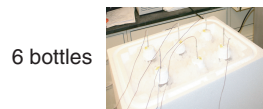


Figure 26.13. Schematic drawing of a FreezeContainer (Zeta Holdings) ([www.zeta.com/bio-und-verfahrenstechnik.html](http://www.zeta.com/bio-und-verfahrenstechnik.html)).



**Figure 27.1.** Freezing in ultra-low-temperature freezers or in dry ice. Product temperature profiles as measured by thermocouples as a function of location in the freezer. (Courtesy of Roland Schmidt.)

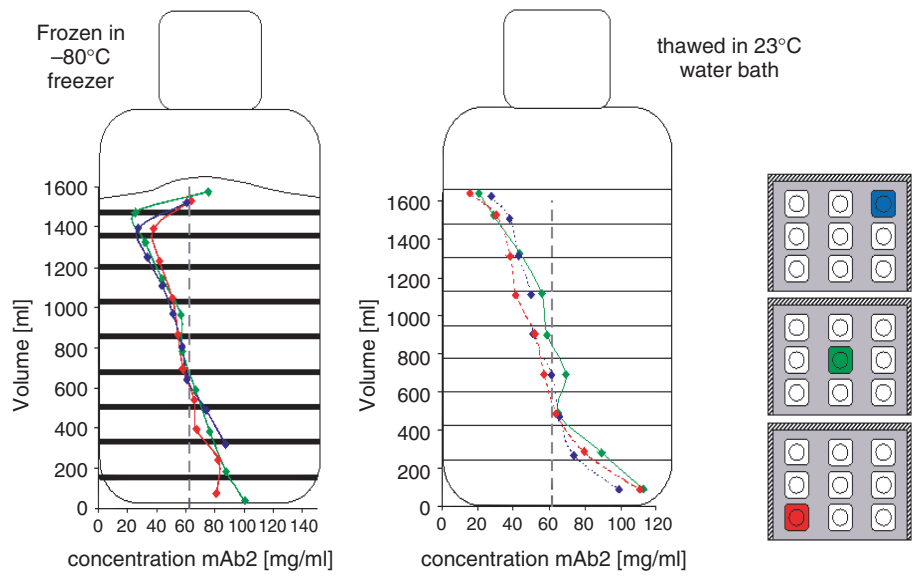
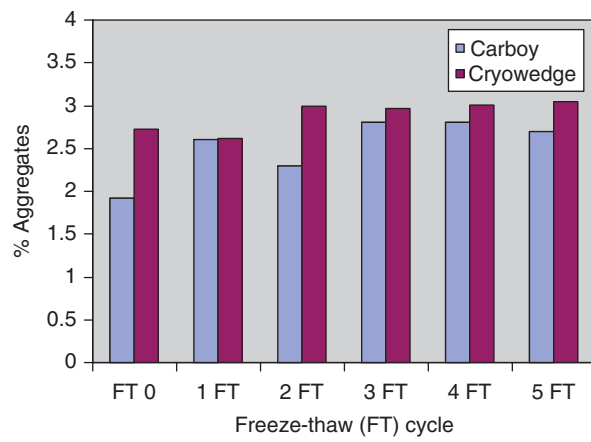


Figure 27.2. Gradient formation in frozen and thawed states. (Courtesy of Roland Schmidt.)



**Figure 27.3.** Results of stability-indicating assays of fusion protein as a function of number of freeze-thaw cycles in (■) carboy (uncontrolled freeze-thaw) and (■) cryowedge (controlled freeze-thaw).

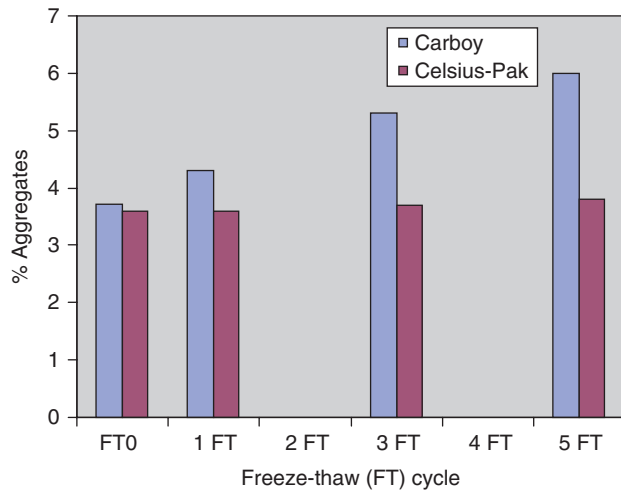
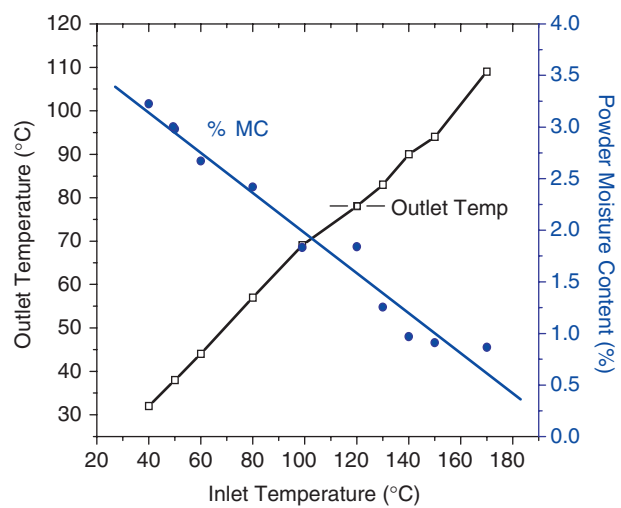
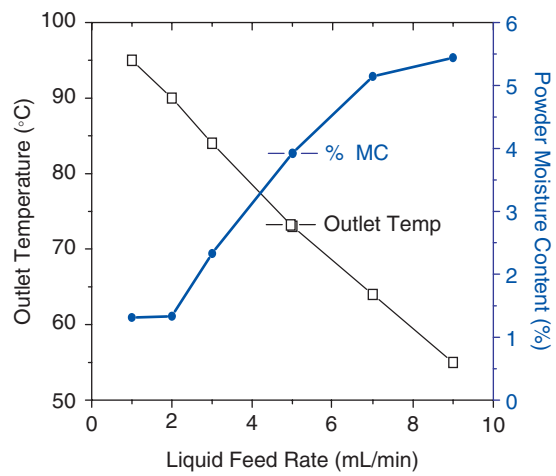


Figure 27.4. Results of stability-indicating assays of peptibody as a function of number of freeze-thaw cycles in (■) carboy (uncontrolled freeze-thaw) and (■) Celsius-Pak (controlled freeze-thaw).

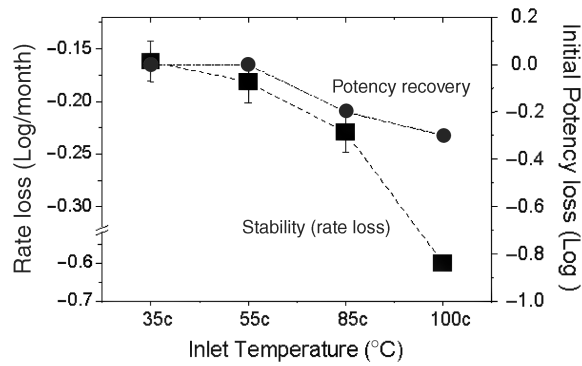


**Figure 28.1.** Effect of drying (inlet) temperature on outlet temperature and moisture content at fixed liquid feed rate of 1 mL/min (Unpublished data.)

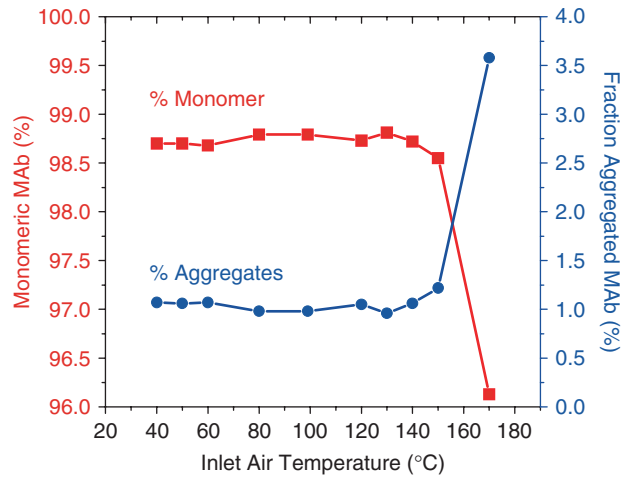




**Figure 28.2.** Effect of liquid feed rate on outlet temperature and moisture content at fixed inlet temperature of 150°C. (Unpublished data.)



(a)



(b)

**Figure 28.6.** (a) Influence of drying temperature on activity recovery and stability of spray-dried live influenza virus; (b) spray drying above the  $T_{\text{unfolding}}$  of a MAb adversely impacted product integrity. Below  $T_{\text{outlet}}$  of 90°C, MAb aggregation process loss was minimal. (Unpublished data.)

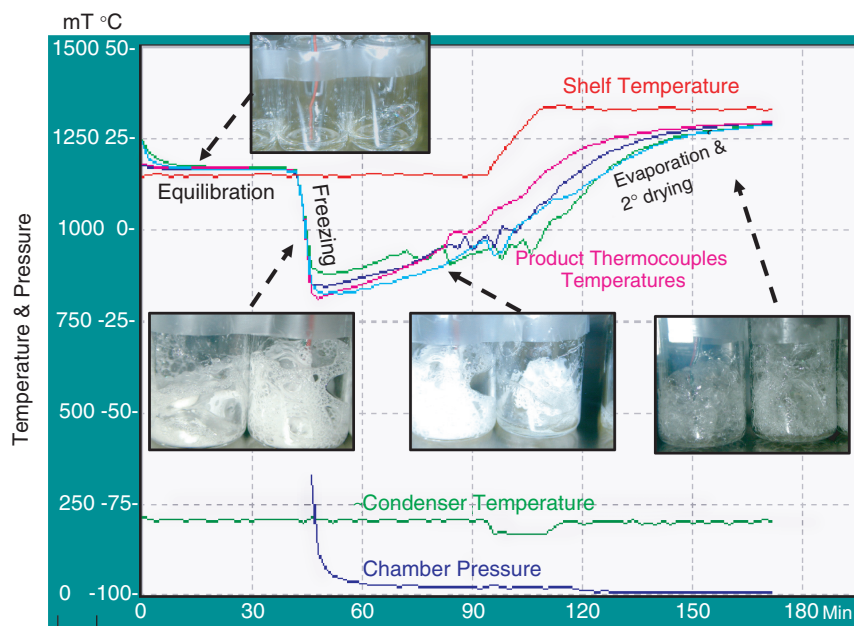
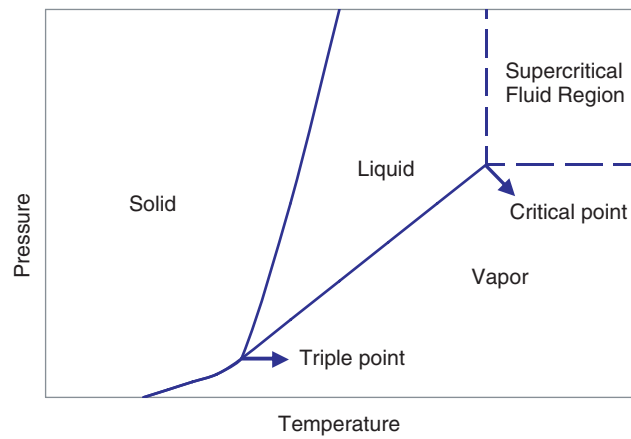


Figure 28.7. Product temperature profile and product foaming during a foam-drying cycle.



**Figure 28.9.** Pressure–temperature phase diagram for a pure component indicating the supercritical region.

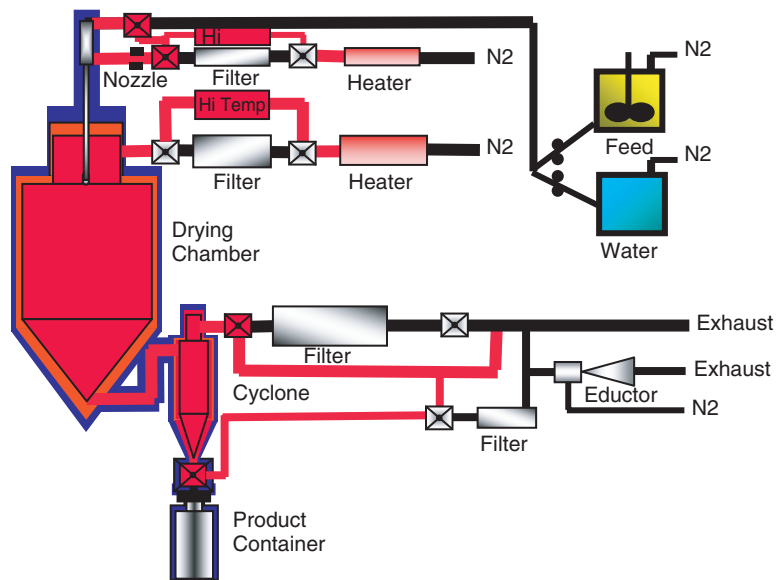
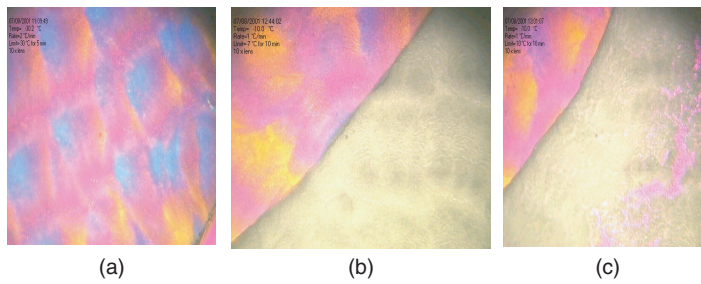
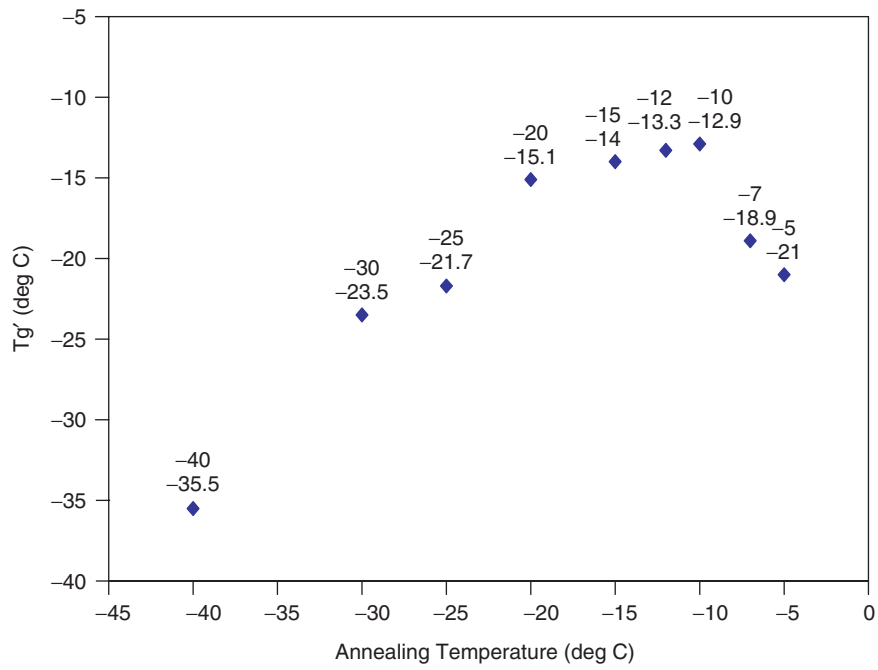


Figure 29.1. An open-mode spray-drying system with an in-place dry-heat sterilization arrangement. (Courtesy of Anhydro A/S, Denmark.)



**Figure 30.2.** Depiction of phenomenon of ice dendrites, drying front with retention of structure and collapse: (a) dendritic ice formation after freezing and before the vacuum is applied; (b) drying with and (c) without retention of the structure.



**Figure 30.5.** Glass transition temperatures  $T_g$  of frozen formulation at various annealing conditions. The data points denote the annealing temperature and  $T_g$ , respectively. From A. Sethuraman and F. Jameel, IBC, 2006.

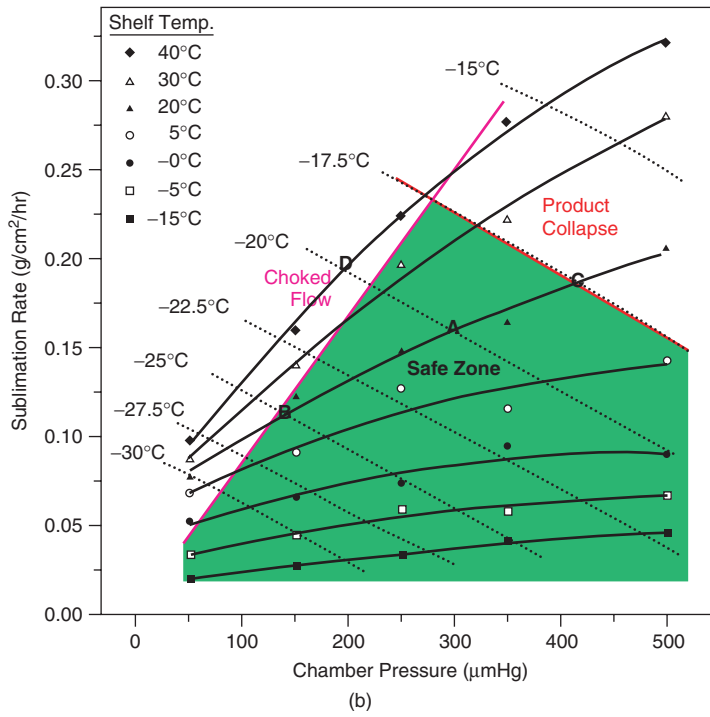
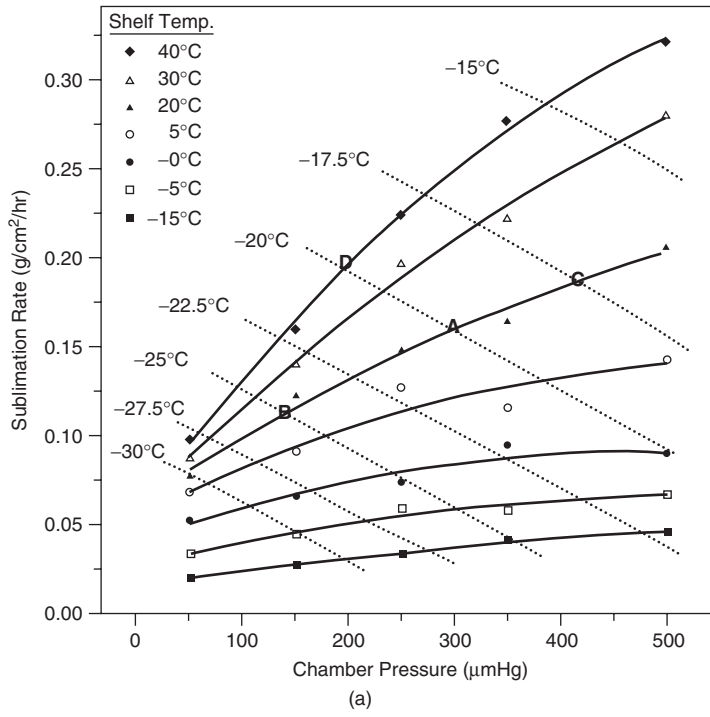
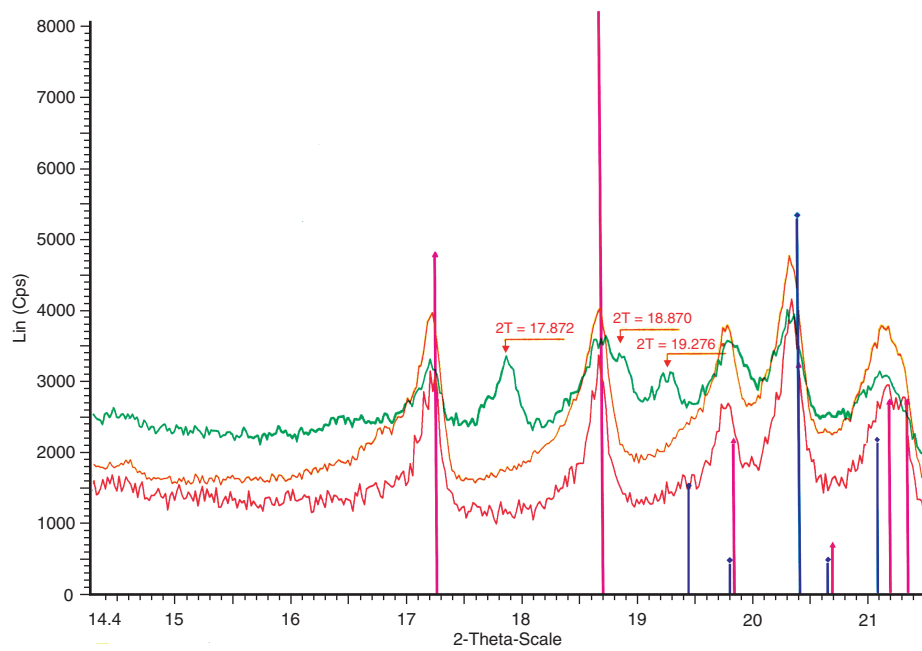


Figure 30.6. (Data from [28, 29]) Sublimation rate versus chamber pressure.







**Figure 30.12.** X-Ray powder diffraction of mannitol depicting the presence of hydrates, which are eliminated through secondary drying at elevated temperature.

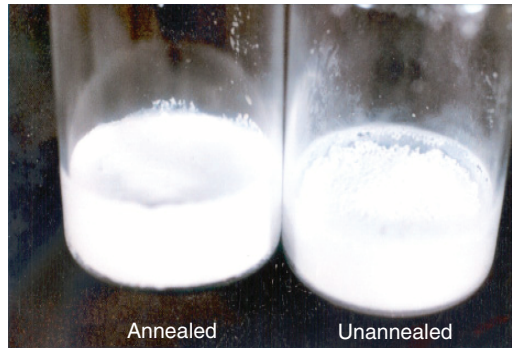
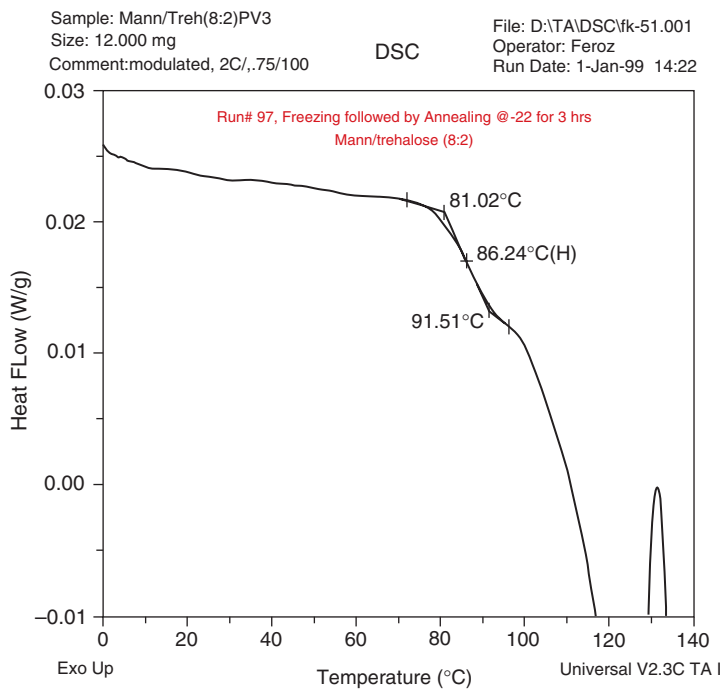
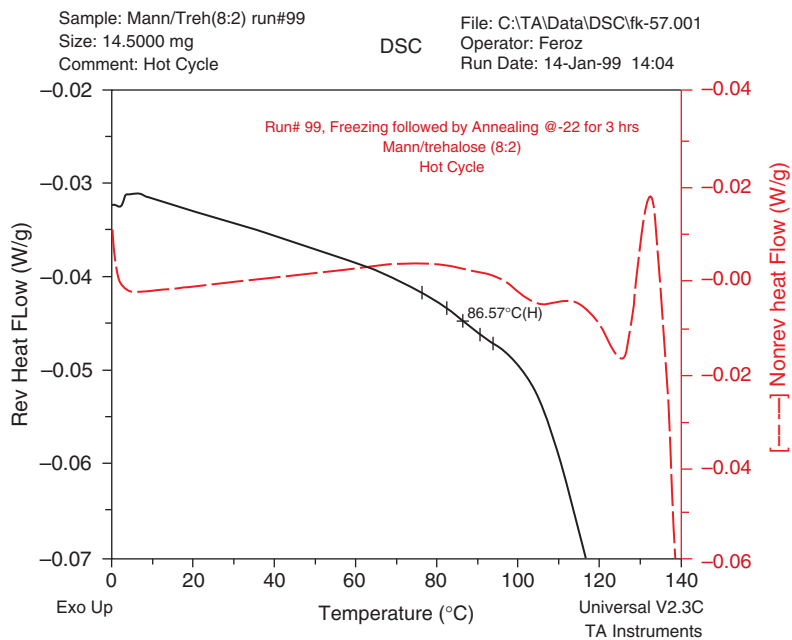


Figure 30.14. Appearance of cake before and after annealing of mannitol and sodium chloride.



(a)



(b)

Figure 30.15. Thermograms depicting increase in  $T_g$  value and no crystallization peak of mannitol and sodium chloride after annealing.

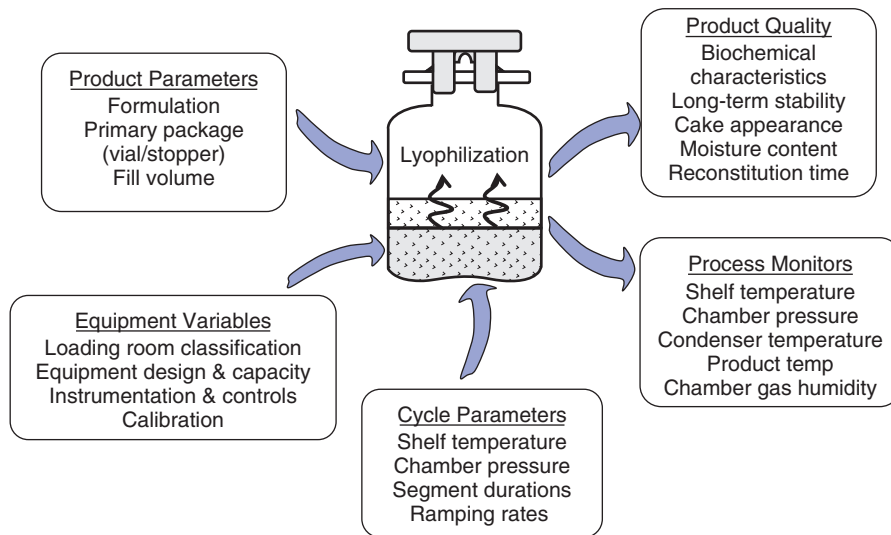
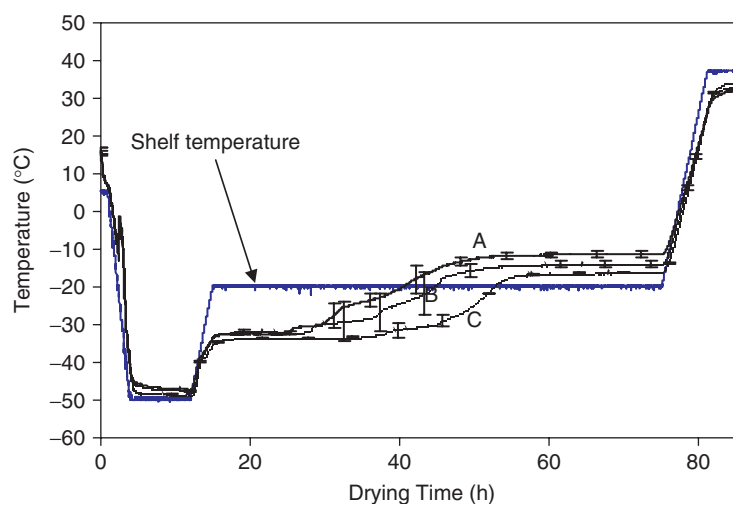
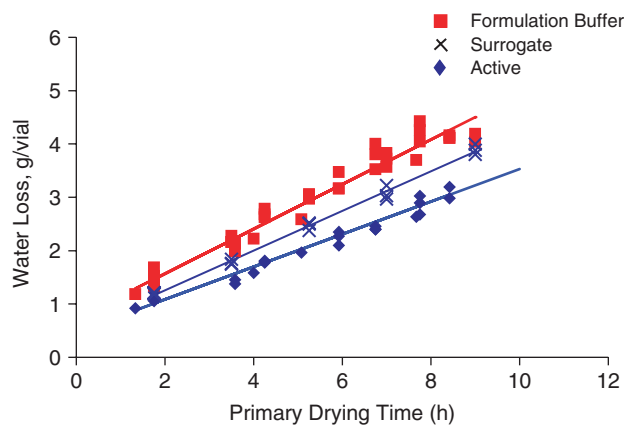


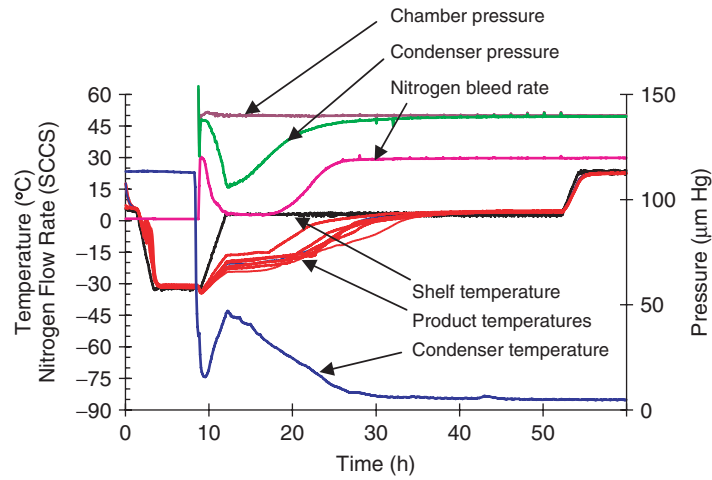
Figure 31.1. Lyophilization process variables.



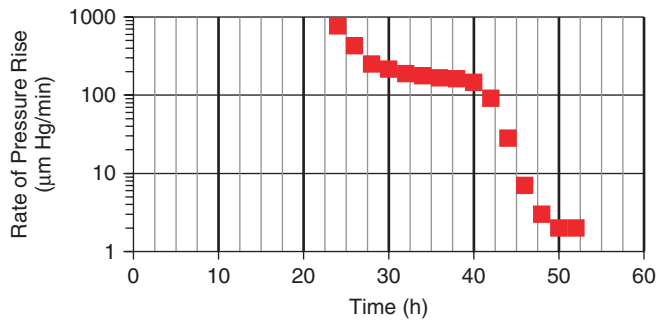
**Figure 31.3.** Product temperature profiles: radiation effect on edge vials. The data were gathered in a 20-ft<sup>2</sup> pilot-scale lyophilizer with transparent acrylic door and stainless-steel walls without wall temperature control. Shelf dimensions were 60 cm wide and 90 cm deep, while the chamber pressure during primary drying was 100 mTorr. Curve A—vials located in the front row facing lyophilizer door; curve B—vials located in the back row closest to the rear wall of the chamber; curve C—vials located in middle rows, roughly in the center of the shelf.



**Figure 31.5.** Comparison of sublimation rates for an antibody formulation. The protein constituted 50% of the total solids content of the formulation. The surrogate had the same solids concentration as the active material.



(a)



(b)

**Figure 31.6.** (a) Temperature and pressure profiles from an engineering run on production scale; (b) pressure rise measurement results from an engineering run on production scale. The corresponding temperature and pressure profiles from this run are presented in (a).



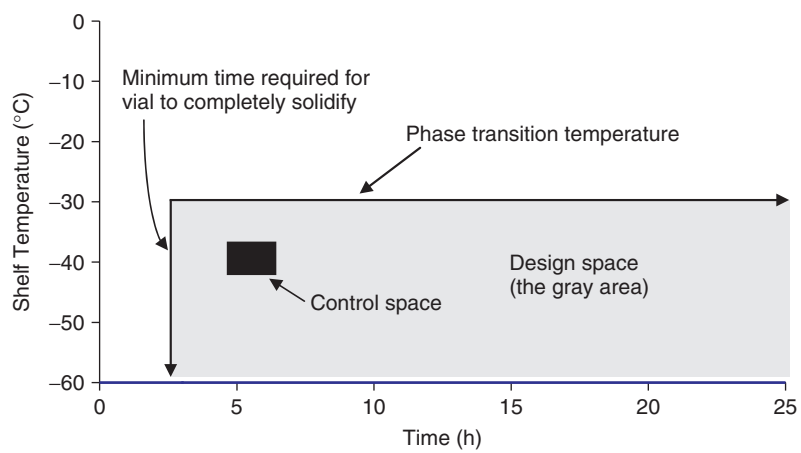
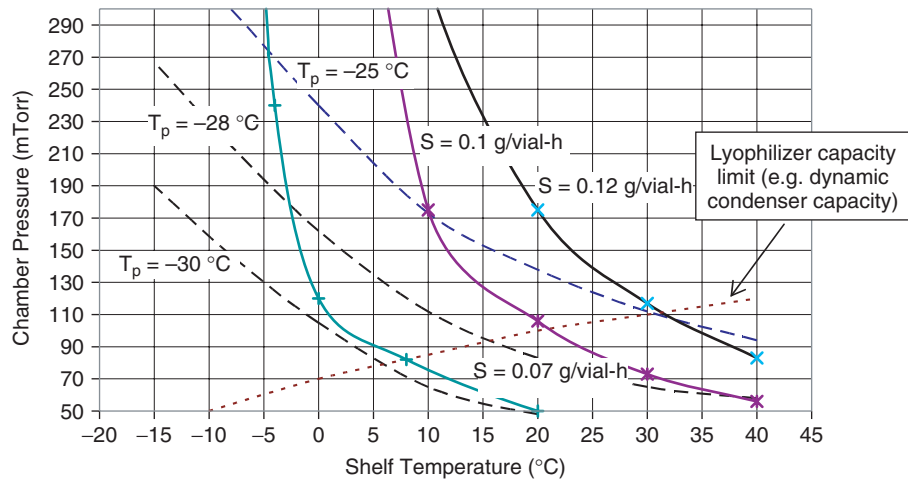
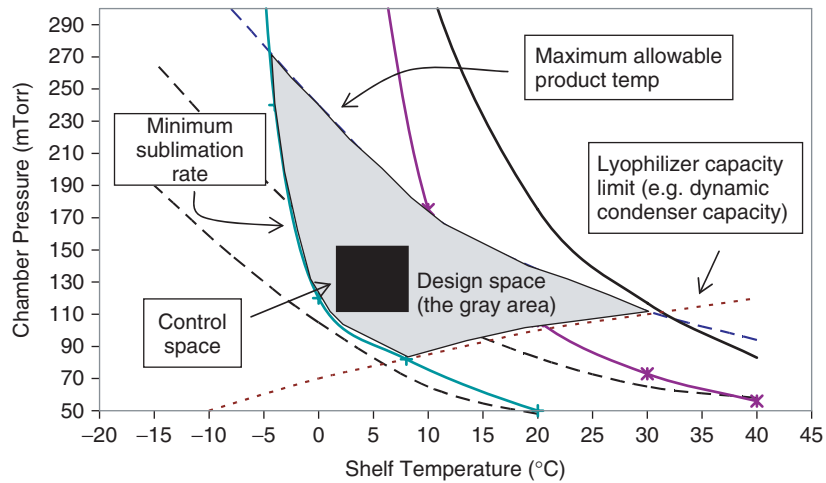


Figure 31.7. Design space for freeze hold. (Chamber pressure is generally inconsequential during freezing and hence not included in the illustration.)



(a)



(b)

**Figure 31.8.** Design space for a fixed primary drying duration (solid lines—constant sublimation rate; dashed lines—constant product temperature; dotted lines—lyophilizer capacity limit).

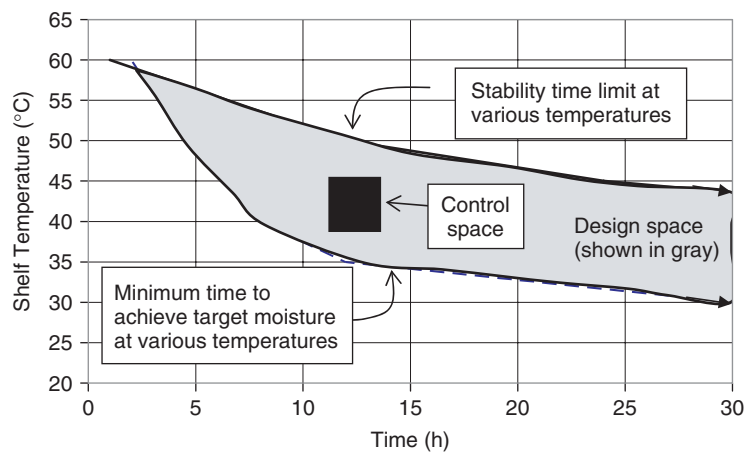
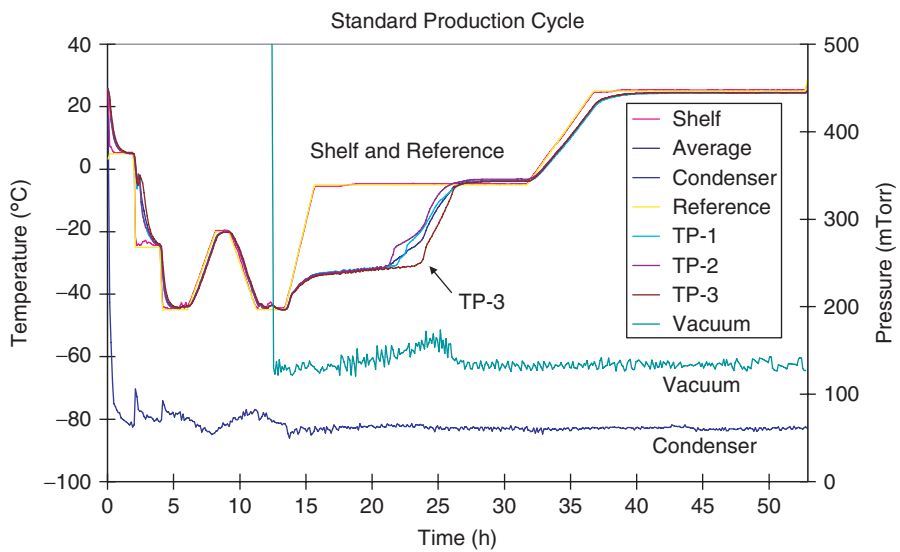


Figure 31.9. Design space for secondary drying hold. (Chamber pressure is generally inconsequential during secondary drying and hence not included in the illustration.)



**Figure 32.1.** Freeze-drying cycle for rFVIII.

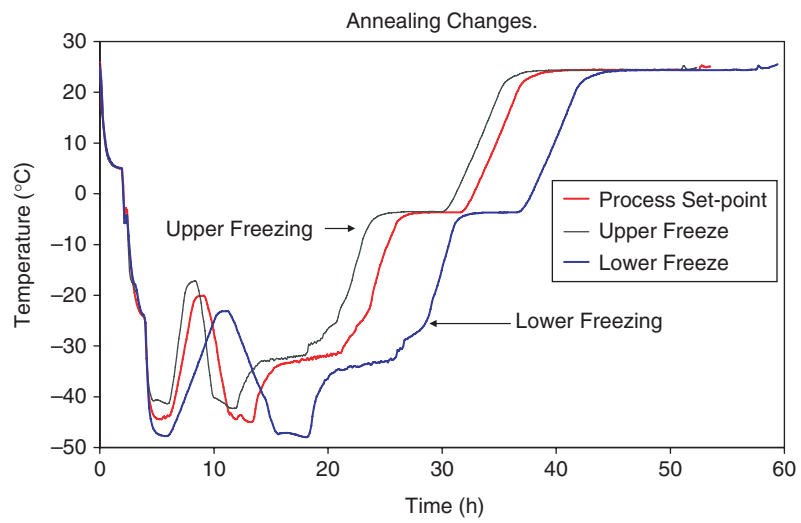


Figure 32.2. Freeze-drying cycle with process parameter changes in freezing phase.

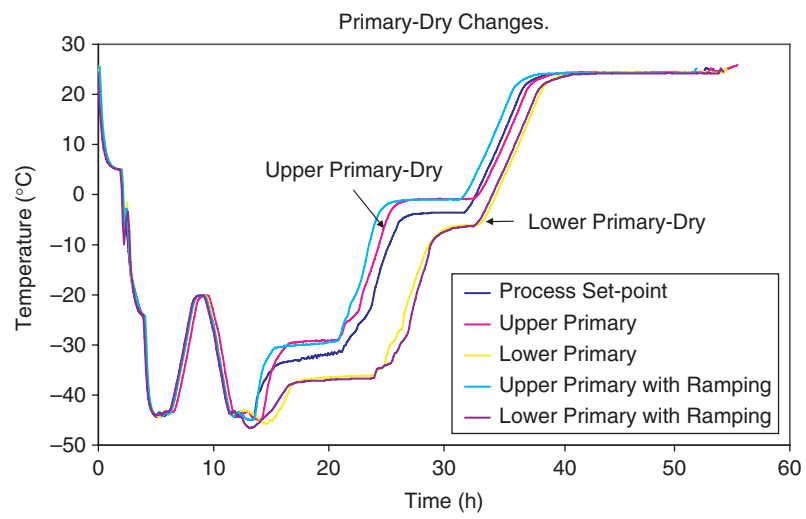
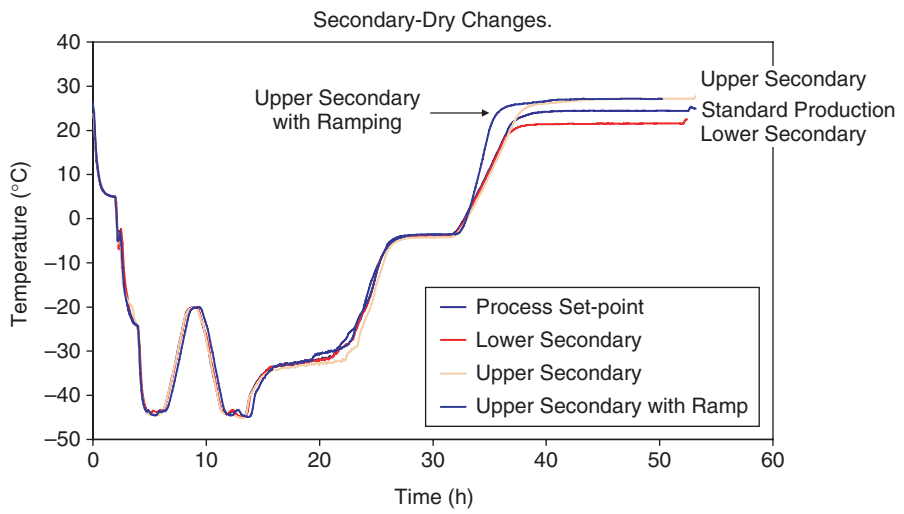


Figure 32.3. Freeze-drying cycles with process parameter changes in primary drying.



**Figure 32.4.** Freeze-drying cycles with process parameter changes in secondary drying.



**Figure 32.5.** Photo of lyophilized product for all 10 cycles. Pictured from left to right: process set point, upper freezing, lower freezing, upper primary, lower primary, upper primary with increased ramping rate, lower primary with decreased ramping rate, upper secondary, lower secondary, and upper secondary with increased ramping rate.



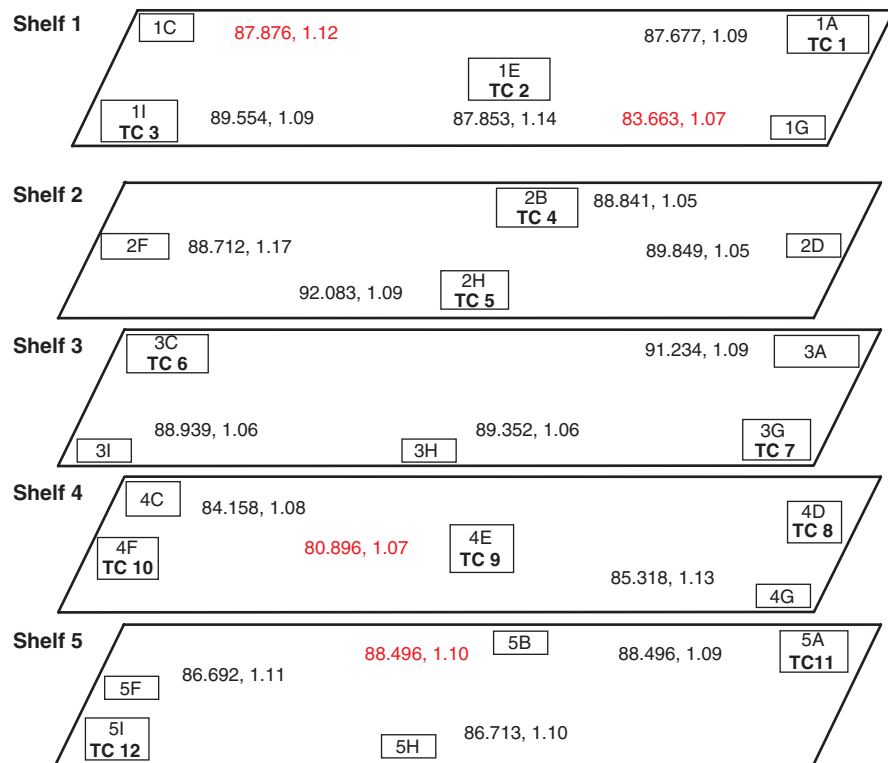


Figure 32.6. Product mapping sample locations, potency results, and moisture results for the top five shelves in a freeze-drier chamber.

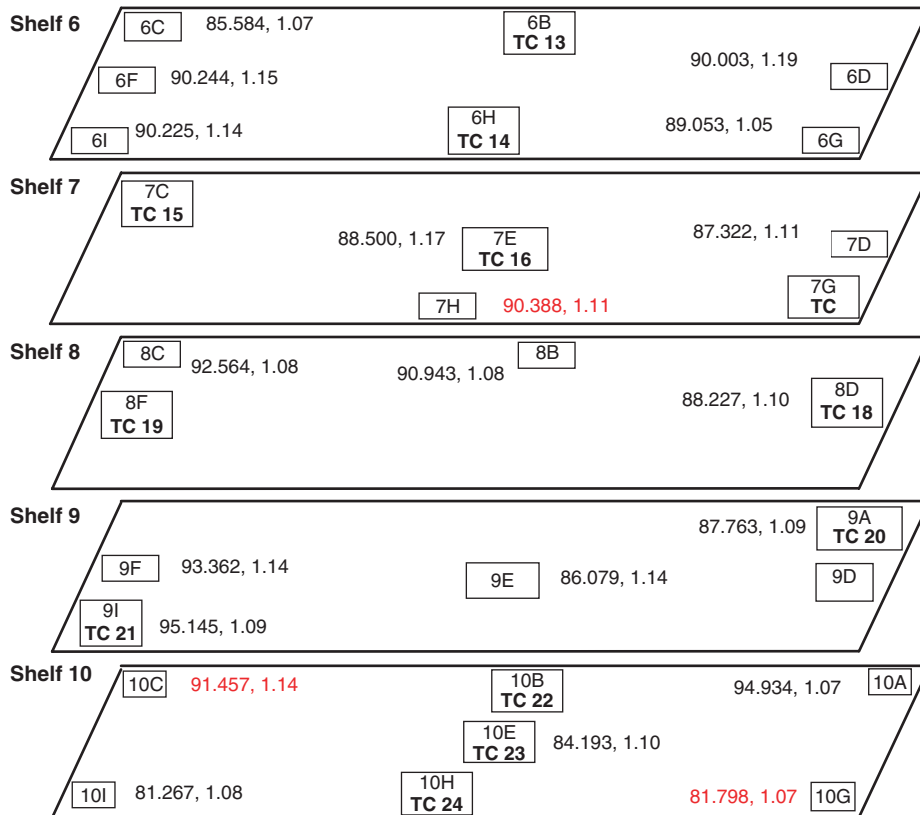
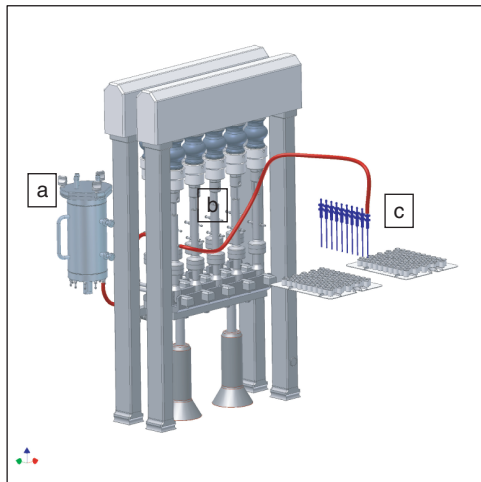


Figure 32.7. Product mapping sample locations, potency results, and moisture results for the bottom five shelves in a freeze-drier chamber.



Figure 33.1. Tabletop piston pump filler.



**Figure 33.2.** Schematic figure of a rotary piston pump filling system: (a) manifold; (b) fill pumps; (c) fill needles.

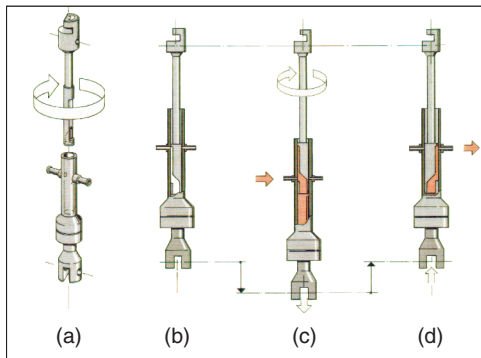


Figure 33.3. Rotary piston pump assembly.

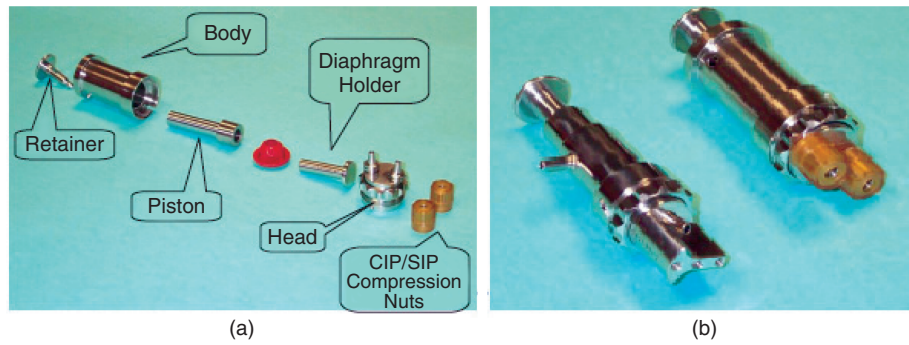
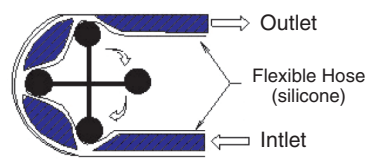
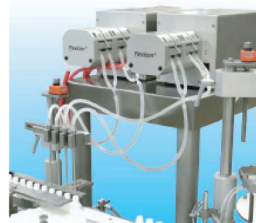


Figure 33.5. (a) Disassembled rolling-diaphragm pump; (b) assembled rolling-diaphragm pump.



(a)



(b)

**Figure 33.6.** Peristaltic pump system: (a) mode of operation; (b) four-head peristaltic filling system.

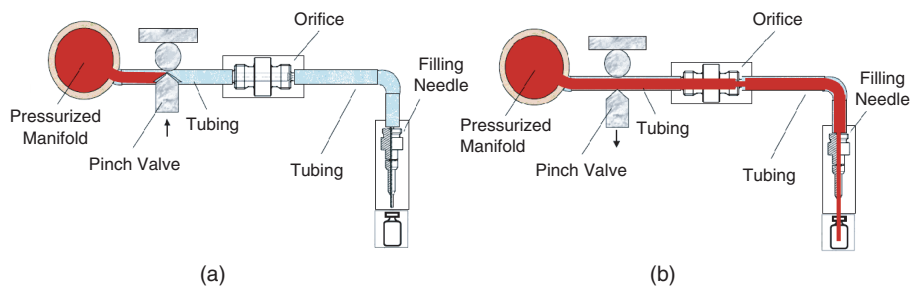


**Figure 33.8.** (a) Product flow through the pinch valve and orifice.



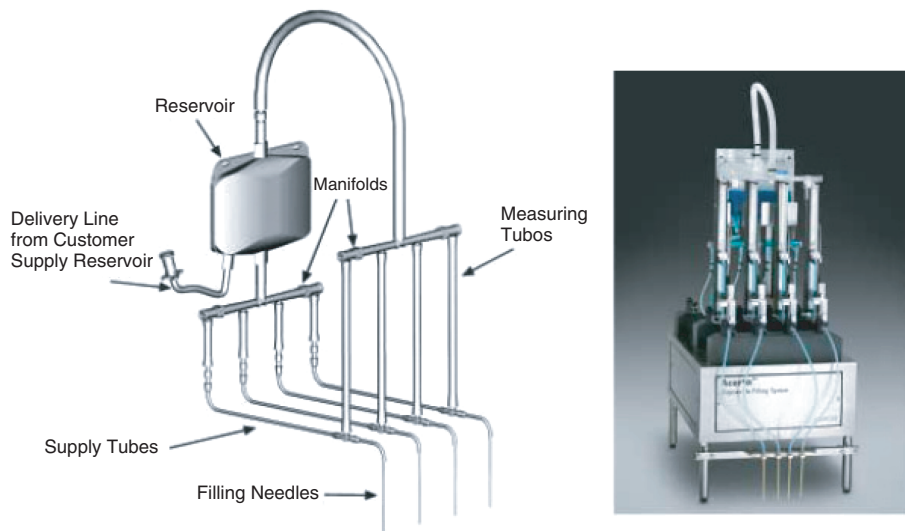


**Figure 33.9.** A disposable filling system showing the disposable reservoir, tubing, and needle assembly along with hardware for mounting on a filling line [4].

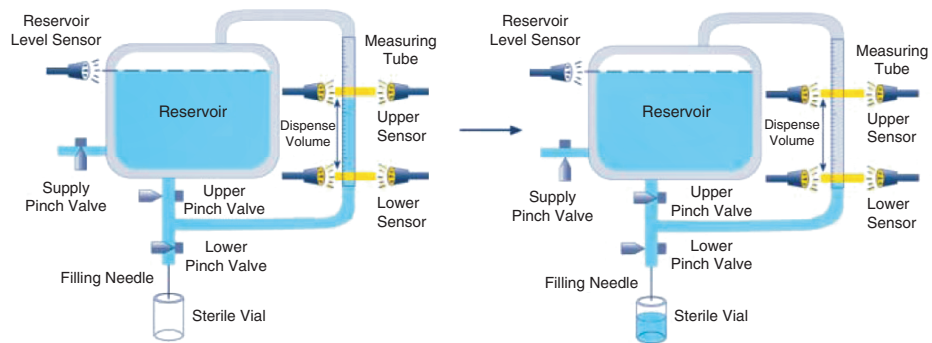
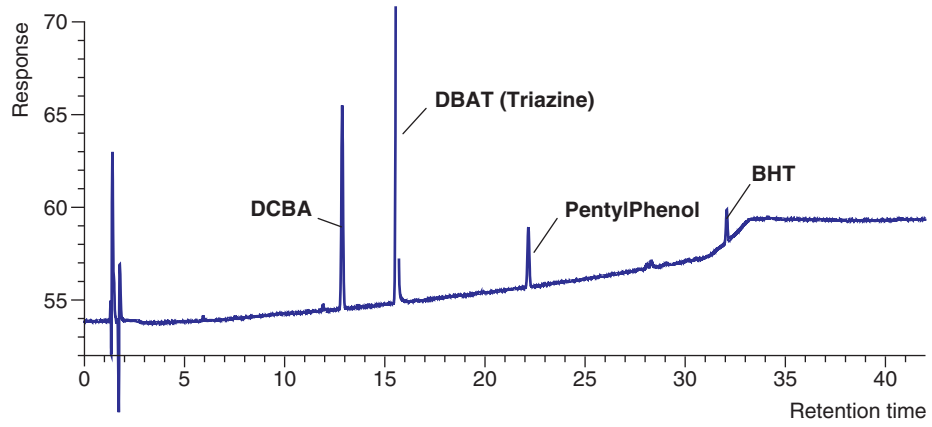


Figure 33.10. A disposable filling system operation; charging of the measuring tube and subsequent dispensing of the sterile product through the filling needles [4].



**Figure 34.3.** Chromatogram of reference compounds covering a  $\log D$  values from  $-0.34$  to  $5.3$ .

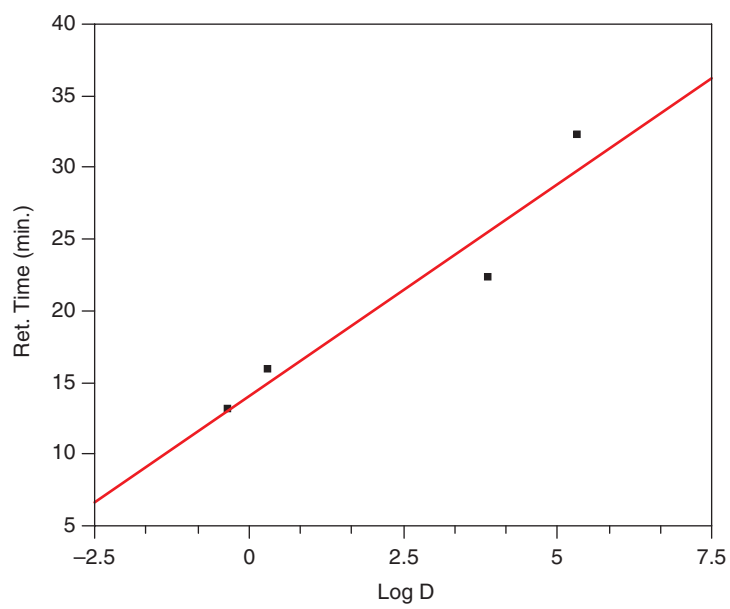


Figure 34.4. Comparison between  $\log D$  and retention time values for reference compounds.

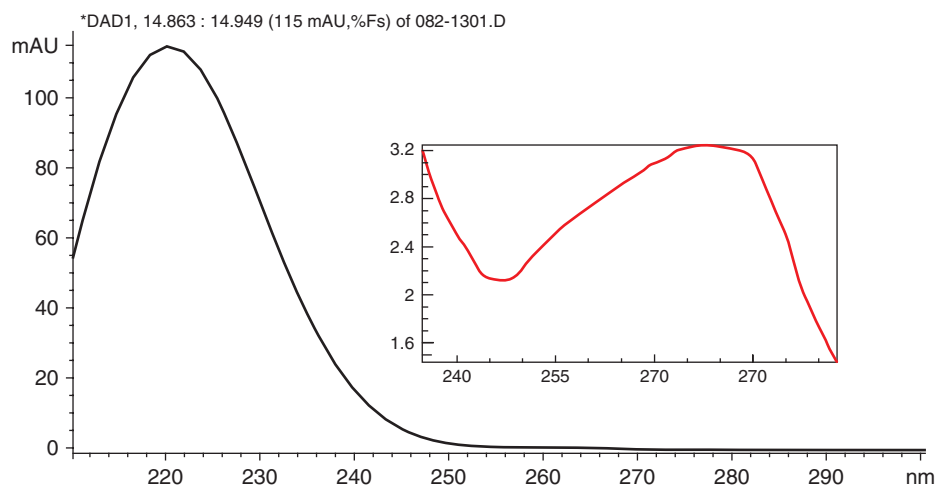
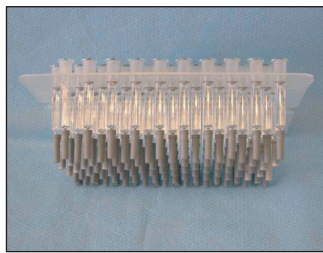


Figure 34.12. Ultraviolet spectral scan of detected extractable compound.



Figure 36.1. Photo of 0.5-mL staked needle (top), 1-mL-long staked needle (middle), and 2.25-mL luer tip syringe barrels.

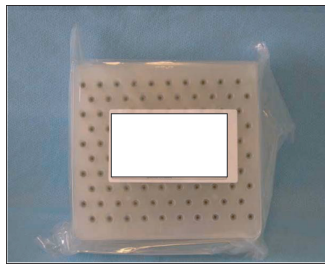


(a)



(b)

Figure 36.2. Photos of 1-mL-long staked needle syringes in nested, ready-to-fill format (a) and unprocessed bulk format (b).



(a)



(b)

Figure 36.3. Ready-to-use 1-mL-long pistons in nested (a) and bagged (b) formats.





Figure 36.4. A 2-ml vial–stopper–seal system showing materials of construction: borosilicate glass vial, elastomer stopper (with or without barrier coating), and aluminum crimp overseal.

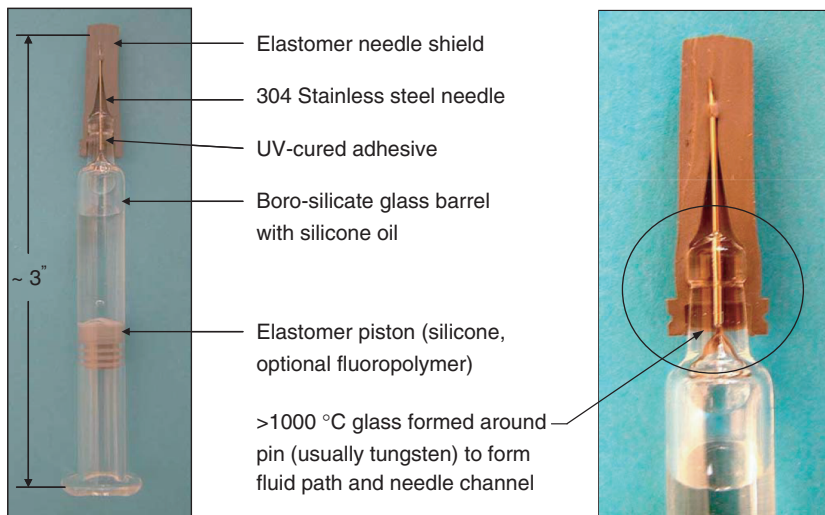


Figure 36.5. A 1-mL-long staked needle syringe system showing direct-contact materials.

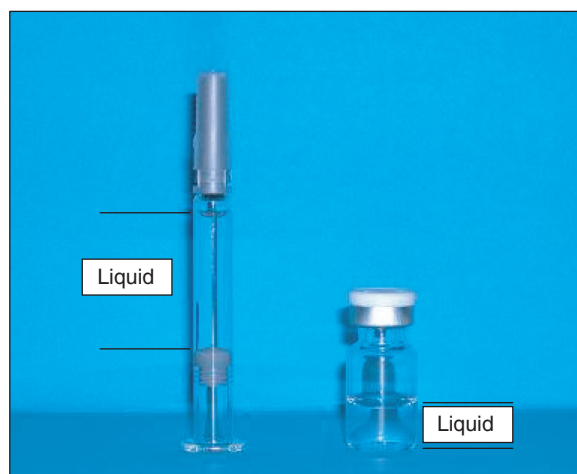
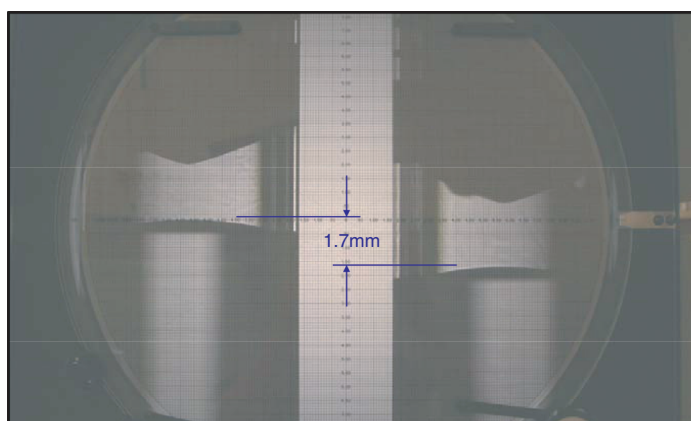


Figure 36.6. A 1-mL-long prefilled syringe and 2-ml vial—both with 1 mL fill showing differences in headspace volume and wetted container surface area.



**Figure 36.7.** Optical comparator image (20 $\times$ ) of the liquid meniscus of 1-mL-long syringes with 1 mL fill volume showing the effect of barrel inner diameter on apparent fill level. The syringe on the left is near minimum specification for barrel inner diameter. The syringe on the right is near the maximum specification.



**Figure 36.8.** A 1-mL-long syringe barrel after breaking off the tip at the shoulder. The resulting hole in the barrel is large enough that product fluid flow resistance is no longer a factor when measuring glide force.

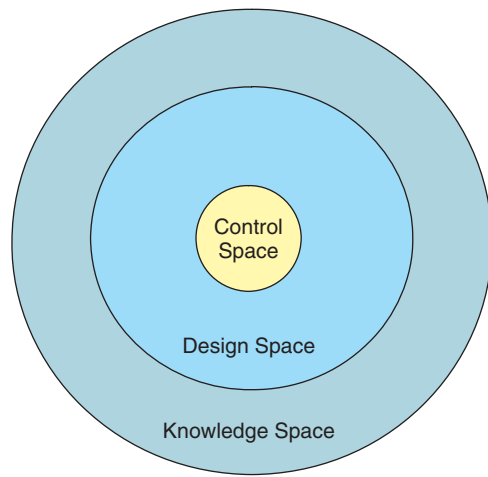
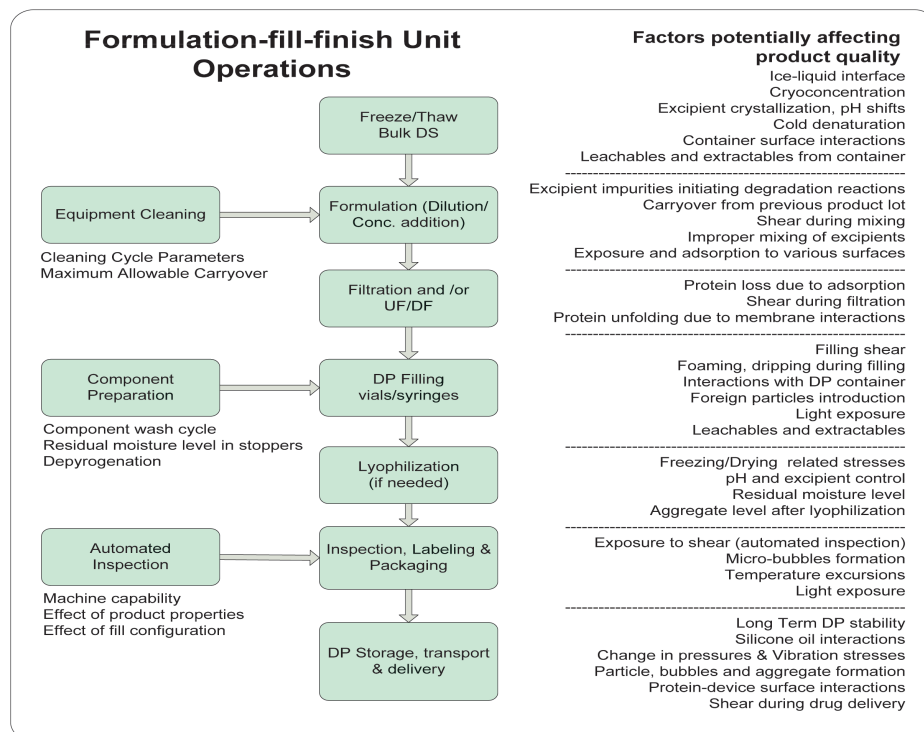
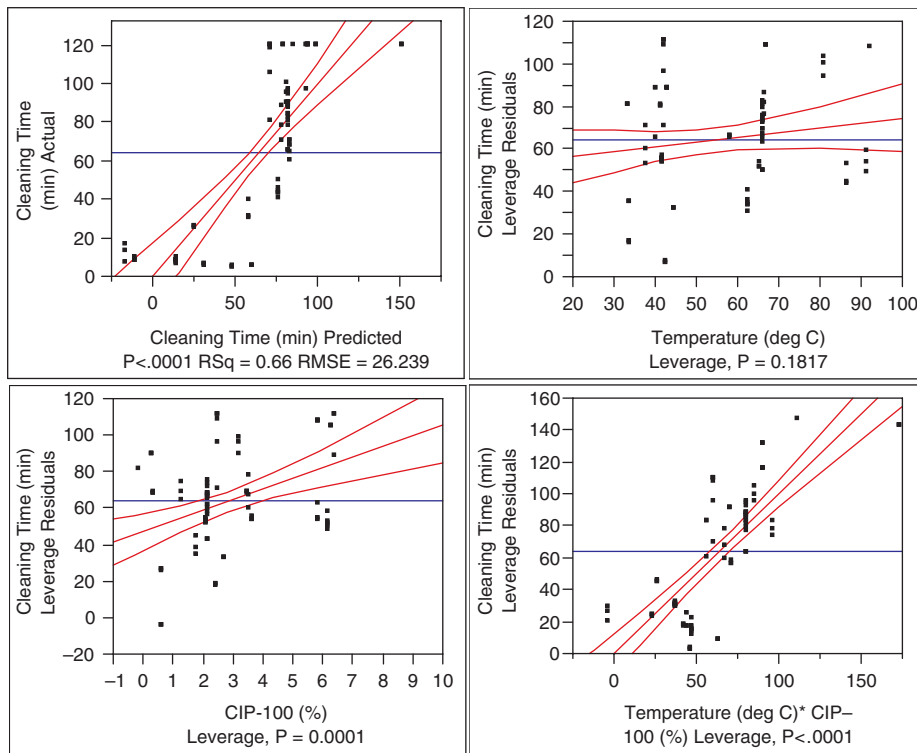


Figure 37.1. Schematic representation of the control, design, and knowledge spaces.



**Figure 37.2.** Overview of formulation, fill, and finish operations and process conditions that can impact product quality during manufacturing.



**Figure 37.3.** Leverage plots for two key parameters: Temperature and Concentration of cleaning solution. The two parameters are strongly coupled as shown by the significance of the cross interaction term.



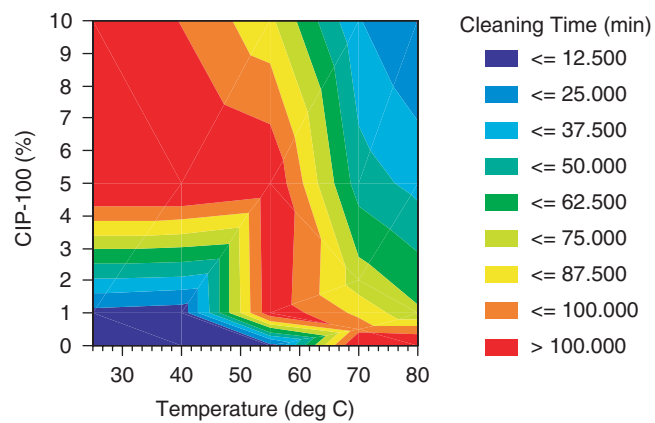


Figure 37.4. Design space characterization for cleaning time with respect to two parameters: Cleaning fluid Temperature and Concentration.